2023-03

Implications of second-order wave generation for physical modelling of force and run-up on a vertical wall using wave groups

Mortimer, W

10.1016/j.coastaleng.2022.104259
Coastal Engineering
Elsevier BV

Coastal Engineering 180 (2023) 104259

Contents lists available at ScienceDirect

Coastal Engineering

journal homepage: www.elsevier.com/locate/coastaleng

Implications of second-order wave generation for physical modelling of force and run-up on a vertical wall using wave groups

William Mortimer [a,b], Ross Calvert [c,d], Alessandro Antonini [e], Deborah Greaves [a], Alison Raby [a], Ton S. van den Bremer [c,e,*]

[a] Faculty of Science and Engineering, University of Plymouth, PL4 8AA, UK
[b] JBA Consulting Ltd., Newcastle-upon-Tyne, NE1 5JE, UK
[c] Department of Engineering Science, University of Oxford, OX1 3PJ, UK
[d] School of Engineering, University of Edinburgh, EH9 3FB, UK
[e] Faculty of Civil Engineering and Geosciences, Delft University of Technology, 2628CD, NL

ARTICLE INFO

Keywords:
Second-order
Wave generation
Error waves
Spurious waves
Set-down
Bound long-waves
Wave force
Wave run-up

ABSTRACT

Experiments are contaminated by second-order error waves at sub- and super-harmonic frequencies when first-order wave generation is used. Herein, we investigate by experiment the implications of second-order wave generation theory for dynamic wave force and run-up on a vertical wall in shallow to intermediate water depth ($k_0 d = 0.5 - 1.1$). Results of short-duration experiments using focused wave groups generated according to first- and second-order theory are compared. We isolate linear, sub-, and super-harmonic contributions using combinations of inverted wave group time series and filtering. We derive theoretical predictions for narrow-banded second-order wave groups interacting with a vertical wall and use this to calculate depth-integrated force and run-up on the wall, which show close agreement with measured data. Comparisons reveal that sub-harmonic error waves are increasingly important in shallow depth, increasing wave run-up by up to 67% and dynamic force by up to 75% at $k_0 d = 0.6$ when compared to the case of correct (second-order) generation in a relatively short flume.

1. Introduction

Coastal communities are increasingly reliant on engineered protection from wave-induced flooding (IPCC, 2019; Young and Ribal, 2019; Haigh et al., 2020; Vousdoukas et al., 2020; Taherkhani et al., 2020). Critical design parameters of such protection include the dynamic force and run-up induced by large waves. Dynamic wave force is the horizontal force exerted on a structure during a wave-structure interaction which excludes the hydro-static force (Goda, 2010), and run-up is the maximum elevation that waves reach above the still-water level (Sorensen, 2005). Excessive wave force can lead to structural failure (e.g., Dawson et al., 2016) and excessive run-up can lead to overtopping and flooding (Goda, 2010).

Run-up associated with the largest waves of a given sea state has primary influence on overtopping volumes of a vertical structure (Van der Meer et al., 2018) and therefore requires accurate estimation by coastal engineers. Present understanding of coastal wave-structure interactions has been gained through large databases of experimental, numerical, and field data, which has been used to inform design guidance such as the EurOtop manual (Pullen et al., 2007), later revised by Van der Meer et al. (2018). Experiments and simulations have historically been conducted with irregular wave trains, where long-duration simulations ensure a statistically extreme wave occurs and provide reasonable estimations of mean overtopping discharge. Yet, in finite-size basins, this approach can be affected by wave reflections and thus requires effective reflection compensation. A short-duration design wave, commonly in the form of a focused wave group, is a complimentary approach to recreate extreme wave-structure interactions in a time-efficient and repeatable manner, prior to wave reflections being measured (e.g., Borthwick et al., 2006; Hofland et al., 2014). This approach is well established in the context of offshore engineering, within the NewWave/Quasi-Determinism (QD) framework (Boccotti, 1983; Tromans et al., 1991; Taylor and Williams, 2004), and increasingly used in shallow-water coastal response investigations (Borthwick et al., 2006; Hofland et al., 2014; Orszaghova et al., 2014; Antonini et al., 2017). Whittaker et al. (2016) demonstrated that focused wave groups provide a valid model of pre-breaking waves in relatively shallow depths. Whittaker et al. (2018) provided further insight by showing focused

* Corresponding author at: Faculty of Civil Engineering and Geosciences, Delft University of Technology, 2628CD, NL.
E-mail address: t.s.vandenbremer@tudelft.nl (T.S. van den Bremer).

https://doi.org/10.1016/j.coastaleng.2022.104259
Received 23 March 2022; Received in revised form 15 November 2022; Accepted 26 November 2022
Available online 2 December 2022

wave groups are a robust method to investigate run-up and wave-induced force in coastal water depths. Karmpadakis and Swan (2020) found that wave groups, specifically those of the NewWave/QD-type, give a good representation of all but the most extreme free surface in shallow water, at which point high-order non-linear terms become dominant.

Wave interaction with a vertical wall is a classical problem in coastal engineering, given the abundance of such structures forming seawalls and quays in ports and harbours providing wave protection and safe berthing (Fenton, 1985; Allsop et al., 1996). Goda (1975) and subsequently (Goda, 2010) provides widely used formulae to calculate dynamic, non-impulsive wave loading on vertical caisson breakwaters. The empirical formulae can be applied to different wave conditions: i.e., standing, non-breaking and breaking waves (after Takahashi's (2002) extension). Oumeraci et al. (2001) proposed predictive tools and methods for quasi-static and impulsive loading as an outcome of the European PROVERBS research collaboration (Allsop et al., 1996). Cuomo (2005) added further insight with a review of the prediction methods, particularly for wave-induced forces on caisson and vertical seawalls. Cuomo et al. (2010) experimentally investigated the effect of scaling on quasi-static and impulsive wave loading on vertical seawalls.

The wave interaction with a vertical wall has first been investigated analytically at second order in steepness using a broad-banded frequency-summation approach by Romolo and Arena (2008), who derived the second-order summation (i.e., super-harmonic) and difference (i.e., sub-harmonic) terms of a Gaussian wavepacket reflecting on a vertical wall. Romolo and Arena (2008) found an increase in wave run-up due to second-order difference standing-wave pattern against the wall. The derivation was then extended to three dimensions by Romolo and Arena (2013), further exploring the second-order effect on wave crests and troughs, before run-up and pressure were validated against a variety of wave conditions, directions, and spreading functions in three-dimensional basin experiments. Sun and Zhang (2017) formulated the run-up problem slightly differently whilst arriving at similar results to Romolo and Arena (2013) for the second-order formulation of three-dimensional waves interacting with a vertical wall. The effects of angle of incidence, wave steepness, focal positions, water depth, and frequency bandwidth on the run-up were then studied. Finally, Laface et al. (2018) compared the derivations of Romolo and Arena (2008) and Sun and Zhang (2017) within a natural wind-driven flume generating irregular waves with a JONSWAP spectrum to find a significant increase of run-up compared with the Rayleigh distribution.

Wave generation using first-order theory gives rise to free error waves, at higher-order, both at sub- and super-harmonic frequencies, which contaminate the wave field (Barthel et al., 1983; Schäffer, 1996; Baldock et al., 2000; Janssen et al., 2003; Van Dongeren et al., 2003; Battjes et al., 2004; Moura and Baldock, 2019; Eldrup and Andersen, 2019; Martins et al., 2021; Mortimer et al., 2022). Free error waves are formed as an instantaneous compensation to a mismatch between depth-dependent water kinematics and first-order wavemaker displacement. Sub-harmonic error waves travel faster than the first-order wave group, and super-harmonic error waves slower. In wave flume experiments, sub-harmonic error waves arrive at the domain of interest first, before the first-order and second-order super-harmonic waves, and therefore represent the most persistent challenge. Second-order error waves, particularly at sub-harmonic frequencies, can significantly affect wave run-up and overtopping results (Hunt, 2003; Orszaghova et al., 2014).

Second-order correct wave generation theory is well established (Barthel et al., 1983; Klopman and Van Leeuwen, 1990; Schäffer, 1996; Van Leeuwen and Klopman, 1996) and has been implemented partially or completely in different relative water depths (Barthel et al., 1983; Van Leeuwen and Klopman, 1996; Orszaghova et al., 2014; Sriram et al., 2015; Fang et al., 2020; Martins et al., 2021; Mortimer et al., 2022). However, experimental investigations carried out with first-order generation remain prolific. Moreover, even in experiments with second-order generation implemented, the second-order sub-harmonic bound waves are often generated incorrectly due to constraints on the extent of wavemaker displacement (e.g., Whittaker et al., 2017, 2018). Orszaghova et al. (2014) demonstrated numerically that experimental investigations, which do not apply second-order corrections correctly, may be affected by the presence of second-order error waves.

The present work investigates the implications of using first- and second-order wave generation theory for dynamic wave force and wave run-up experiments on a vertical wall using focused wave groups. We make use of a piston-type wavemaker, developed by Edinburgh Designs Ltd. with a long paddle displacement range. The long displacement range permits the application of second-order wave generation in shallow-water depths, where a significant sub-harmonic paddle displacement range is required (Mortimer et al., 2022). We use second-order wave generation theory derived by Van Leeuwen and Klopman (1996) to formulate the required second-order correct displacement for mitigating sub- and super-harmonic free error waves. The wavemaker and application of Van Leeuwen and Klopman's theory is described in detail by Mortimer et al. (2022). Herein, we derive the theoretical contributions of force and run-up from first-order and second-order sub- and super-harmonic terms, including interaction terms. We compare these predicted terms to experimental measurements to assess the implications of first- and second-order wave generation.

This paper is laid out as follows. We first derive our second-order theoretical results for run-up and dynamic wave force in Section 2. This is followed by description of the intermediate to shallow-water wave-flume experiments in Section 3, before comparison between theory and experimental measurements and their dependence on the order of wave-generation is made in Section 4. Finally, conclusions are drawn in Section 5.

2. Second-order theory for wave groups reflecting on a vertical wall

2.1. Governing equations and boundary conditions

We consider a two-dimensional body of water of depth d with a coordinate system (x, z), where x denotes the horizontal coordinate, and z the vertical coordinate measured from the undisturbed water level upwards. Inviscid, incompressible, and irrotational flow is assumed and, as a result, the velocity vector can be defined as the gradient of the velocity potential $\mathbf{u} = \boldsymbol{\nabla}\phi$. The governing equation within the domain of the fluid is then Laplace:

$$\nabla^2\phi = 0 \quad \text{for} \quad -d \le z \le \eta(x,t), \tag{1}$$

where $\eta(x,t)$ denotes the free surface. The kinematic and dynamic free-surface boundary conditions are, respectively:

$$w - \frac{\partial\eta}{\partial t} - u\frac{\partial\eta}{\partial x}, \quad g\eta + \frac{\partial\phi}{\partial t} + \frac{1}{2}|\boldsymbol{\nabla}\phi|^2 = 0 \quad \text{at } z = \eta(x,t), \tag{2a,b}$$

where gravity g acts in the negative z-direction and $|\boldsymbol{\nabla}\phi|^2 = u^2 + w^2$. A vertical wall is placed at $x = x_w$, so that $u = \partial\phi/\partial x = 0$ at $x = x_w$. Finally, there is a no-flow bottom boundary condition requiring that $w = \partial\phi/\partial z = 0$ at $z = -d$. The pressure at any depth underneath the waves is given by the unsteady Bernoulli equation:

$$p = -\rho\left(\partial_t\phi + \frac{1}{2}|\boldsymbol{\nabla}\phi|^2 + gz\right) \quad \text{for} \quad -d < z < \eta, \tag{3}$$

where ρ is the density of water.

We consider only the first two orders in a perturbation expansion in steepness ϵ, so we have for ϕ and η (and similarly for all other variables),

$$\phi = \phi^{(1)} + \phi^{(2)} + \mathcal{O}(\epsilon^3), \quad \eta = \eta^{(1)} + \eta^{(2)} + \mathcal{O}(\epsilon^3), \tag{4a,b}$$

where the superscripts denote the order in steepness ϵ. By retaining terms up to second order in the steepness of the waves, the two free-surface boundary conditions in (2a,b) can be combined into two

forcing equations for the second-order potential and surface elevation (Longuet-Higgins and Stewart, 1964):

$$\left(\frac{\partial}{\partial z}+\frac{1}{g}\frac{\partial^2}{\partial t^2}\right)\phi^{(2)}|_{z=0} = \frac{\partial}{\partial x}\left(u^{(1)}\Big|_{z=0}\eta^{(1)}\right)-\frac{1}{g}\frac{\partial}{\partial t}\left(\frac{\partial^2\phi^{(1)}}{\partial z\partial t}\Big|_{z=0}\eta^{(1)}+\frac{1}{2}|\nabla\phi^{(1)}|^2_{z=0}\right), \tag{5}$$

$$\eta^{(2)}=\frac{-1}{g}\left(\frac{\partial\phi^{(2)}}{\partial t}\Big|_{z=0}+\left(\frac{\partial^2\phi^{(1)}}{\partial z\partial t}\Big|_{z=0}\eta^{(1)}+\frac{1}{2}|\nabla\phi^{(1)}|^2\Big|_{z=0}\right)\right). \tag{6}$$

Similarly, we obtain for pressure at any depth, $p=p^{(0)}+p^{(1)}+p^{(2)}+\mathcal{O}(\epsilon^3)$, by expanding (3),

$$p=-\rho\left(gz+\partial_t\phi^{(1)}+\partial_t\phi^{(2)}+\frac{1}{2}|\nabla\phi^{(1)}|^2\right)\ \text{for}\ -d<z<\eta, \tag{7}$$

where the zeroth-order pressure is the hydrostatic pressure.

2.2. First-order in steepness

Herein, we assume wave groups based on a narrow-banded (and later Gaussian) spectrum, consistent with the classical second-order results for isolated groups by Mei (1989) and the accompanying wavemaker theory by Van Leeuwen and Klopman (1996) (and Calvert et al., 2019). The presently used wave groups can be expressed as a slow modulation in space and time by an envelope of a carrier wave with frequency ω_0 and wavenumber k_0, satisfying the linear dispersion relationship $\omega_0^2=gk_0\tanh(k_0d)$. Combination of the incident and reflected waves gives for the first-order surface elevation:

$$\eta^{(1)}(x,t)=A_\mathrm{I}(X_\mathrm{I})\cos(\varphi_\mathrm{I})+A_\mathrm{R}(X_\mathrm{R})\cos(\varphi_\mathrm{R}), \tag{8}$$

where $\varphi_\mathrm{I}=k_0x-\omega_0t+\mu_\mathrm{I}$ and $\varphi_\mathrm{R}=-k_0x-\omega_0t+\mu_\mathrm{R}$, indicating the incident (I) and reflected (R) waves travel in the positive and negative x-directions, respectively. Using multiple scales, the envelopes A_I and A_R vary on the slow scales $X_\mathrm{I}=\delta(x-c_{g,0}t)$ and $X_\mathrm{R}=-\delta(x+c_{g,0}t)$, respectively, where the additional small parameter δ measures the bandwidth of the underlying spectrum. The limit $\delta\to0$ corresponds to monochromatic waves. We only need to consider first-order solutions in steepness up the zeroth order in bandwidth (i.e., $\mathcal{O}(\epsilon^1,\delta^0)$) in order to obtain leading-order solutions for the run-up and force at second order, as consistent with the results in Mei (1989), McAllister et al. (2018), van den Bremer et al. (2019) and Calvert et al. (2019). The corresponding solutions for other relevant first-order quantities are given in Table 1.

To satisfy the no-flow boundary condition at the wall, we require $A_\mathrm{R}(x=x_\mathrm{w})=A_\mathrm{I}(x=x_\mathrm{w})$ and $\mu_\mathrm{R}=\mu_\mathrm{I}$, corresponding to perfect reflection and $\eta^{(1)}_\mathrm{w}=\eta^{(1)}(x=x_\mathrm{w})=2A_\mathrm{w}(t)\cos(\varphi_\mathrm{w})$ with $\varphi_\mathrm{w}=\varphi_\mathrm{I}(x=x_\mathrm{w})=-\omega_0t+\mu_\mathrm{I}$ and $A_\mathrm{w}(t)=A_\mathrm{I}(x=x_\mathrm{w},t)$. To obtain the first-order force on the wall, we simply integrate the first-order pressure from Table 1 and evaluate the result at x_w:

$$F^{(1)}_\mathrm{w}/b=\int_{-d}^{0}p^{(1)}(x=x_\mathrm{w})\mathrm{d}z=\frac{2\rho g\tanh k_0d}{k_0}A_\mathrm{w}(t)\cos(\varphi_\mathrm{w}), \tag{9}$$

where b is the width of the wall. This simply corresponds to twice the force from the incident wave alone.

2.3. Second-order in steepness

2.3.1. Velocity potential

Considering the velocity potential first, we note from substituting the first-order solutions from Table 1 into the right-hand side of (5) that the forcing of (5) on the right-hand side can be decomposed into self-interaction terms ($\sim A_\mathrm{I}A_\mathrm{I}$ and $A_\mathrm{R}A_\mathrm{R}$) and cross-interaction terms ($\sim A_\mathrm{I}A_\mathrm{R}$). We therefore decompose the solution for the second-order potential in the same way:

$$\phi^{(2)}=\phi^{(2)}_\mathrm{I}+\phi^{(2)}_\mathrm{R}+\phi^{(2)}_\mathrm{I,R}. \tag{10}$$

Table 1
First-order solutions ($\mathcal{O}(\epsilon^1,\delta^0)$).

Quantity	Incident (I)	Reflected (R)
φ	$\varphi_\mathrm{I}=k_0\mathrm{x}-\omega_0t+\mu_\mathrm{I}$	$\varphi_\mathrm{R}=-k_0\mathrm{x}-\omega_0t+\mu_\mathrm{R}$
X	$X_\mathrm{I}=\delta(\mathrm{x}-c_{g,0}t)$	$X_\mathrm{R}=-\delta(x+c_{g,0}t)$
$\eta^{(1)}$	$A_\mathrm{I}(X_\mathrm{I})\cos(\varphi_\mathrm{I})$	$A_\mathrm{R}(X_\mathrm{R})\cos(\varphi_\mathrm{R})$
$\phi^{(1)}$	$c_{p,0}A_\mathrm{I}(X_\mathrm{I})\frac{\cosh k_0(z+d)}{\sinh k_0d}\sin(\varphi_\mathrm{I})$	$c_{p,0}A_\mathrm{R}(X_\mathrm{R})\frac{\cosh k_0(z+d)}{\sinh k_0d}\sin(\varphi_\mathrm{R})$
$u^{(1)}$	$\omega_0A_\mathrm{I}(X_\mathrm{I})\frac{\cosh k_0(z+d)}{\sinh k_0d}\cos(\varphi_\mathrm{I})$	$-\omega_0A_\mathrm{R}(X_\mathrm{R})\frac{\cosh k_0(z+d)}{\sinh k_0d}\cos(\varphi_\mathrm{R})$
$w^{(1)}$	$\omega_0A_\mathrm{I}(X_\mathrm{I})\frac{\sinh k_0(z+d)}{\sinh k_0d}\sin(\varphi_\mathrm{I})$	$\omega_0A_\mathrm{R}(X_\mathrm{R})\frac{\sinh k_0(z+d)}{\sinh k_0d}\sin(\varphi_\mathrm{R})$
$p^{(1)}$	$\rho\omega_0c_{p,0}A_\mathrm{I}(X_\mathrm{I})\frac{\cosh k_0(z+d)}{\sinh k_0d}\cos(\varphi_\mathrm{I})$	$\rho\omega_0c_{p,0}A_\mathrm{R}(X_\mathrm{R})\frac{\cosh k_0(z+d)}{\sinh k_0d}\cos(\varphi_\mathrm{R})$

Starting with the super-harmonic terms, as denoted by the superscript +2, we readily obtain the well-known result for the self-interaction terms (e.g., Mei, 1989):

$$\phi^{(+2)}_\mathrm{I}=\frac{3A_\mathrm{I}^2\omega_0}{8}\frac{\cosh(2k_0(z+d))}{\sinh^4(k_0d)}\sin(2\varphi_\mathrm{I}), \tag{11}$$

which simply corresponds to the super-harmonic term for a regular Stokes wave modulated by an envelope $A_\mathrm{I}(X_\mathrm{I})$, and similarly for the reflected wave (upon replacement of I by R in (11)).

By substituting first-order solutions from Table 1 into the right-hand side of (5), it can be shown that the forcing of the cross-interaction term ($\sim A_\mathrm{I}A_\mathrm{R}$) is only a fast function of t and not of x. Because the resulting potential has to satisfy the Laplace equation, the leading-order solution $\phi^{(+2)}_\mathrm{I,R}$ is only a function of fast time t:

$$\phi^{(+2)}_\mathrm{I,R}=-\frac{1}{4}\omega_0A_\mathrm{I}A_\mathrm{R}\left(3+\frac{1}{\tanh^2(k_0d)}\right)\sin(\varphi_\mathrm{I}+\varphi_\mathrm{R}), \tag{12}$$

where $\varphi_\mathrm{I}+\varphi_\mathrm{R}=-2\omega_0t+2\mu_\mathrm{I}$. For completeness, we note that we recover the deep-water limit given by Eq. (26) of McAllister and van den Bremer (2019) (for the case therein when two groups cross at $\Delta\theta=180°$). The sub-harmonic terms, as denoted by the superscript −2, are readily obtained by the well-known mean flow potential for the self-interaction terms (e.g., Calvert et al., 2019); we note an erroneous surplus minus in Eq. (15) of Calvert et al. (2019)):

$$\phi^{(-2)}_\mathrm{I}=\frac{\omega_0\left(1+\frac{c_{g,0}\omega_0}{g\sinh(2k_0d)}\right)}{4\pi\tanh(k_0d)}\int_{-\infty}^{\infty}\widehat{A_\mathrm{I}^2}\frac{\cosh(k(z+d))}{\sinh(kd)}\frac{i\exp(ik\tilde{x}_\mathrm{I})}{1-\frac{kc^2_{g,0}}{g\tanh(kd)}}\mathrm{d}k, \tag{13}$$

where $\tilde{x}_\mathrm{I}=X_\mathrm{I}/\delta$ and $\widehat{|A_\mathrm{I}|^2}=\int_{-\infty}^{\infty}A_\mathrm{I}^2\exp(-ik\tilde{x}_\mathrm{I})\mathrm{d}\tilde{x}_\mathrm{I}$ is the Fourier transform of A_I^2. The analogous result for the reflected wave is given by (13) upon replacement of I by R.

For the cross-interaction term, we can express (5) as

$$\underbrace{\left(\frac{\partial}{\partial z}+\frac{1}{g}\frac{\partial^2}{\partial t^2}\right)}_{=\mathcal{L}}\phi^{(-2)}_\mathrm{I,R}|_{z=0} = \underbrace{\frac{\omega_0^2}{2g}\left(1+\frac{1}{\tanh^2(k_0d)}\right)\frac{\partial}{\partial t}\left(A_\mathrm{I}A_\mathrm{R}\right)\cos(\varphi_\mathrm{I}-\varphi_\mathrm{R})}_{=\mathcal{F}_\mathrm{I,R}}, \tag{14}$$

where $\varphi_\mathrm{I}-\varphi_\mathrm{R}=2k_0x$ includes a fast dependence on x. In the absence of an obvious closed-form solution, we use a bivariate Fourier transform in x and t to solve (14), seeking a solution of the form $\hat{\phi}_\mathrm{I,R}=f(k,\omega)\exp(i(kx+\omega t))\cosh(k(z+d))/\cosh(kd)$, and obtain:

$$\phi^{(-2)}_\mathrm{I,R}=\frac{1}{4\pi^2}\int_{-\infty}^{\infty}\int_{-\infty}^{\infty}\frac{\hat{\mathcal{F}}^{(-2)}_\mathrm{I,R}}{-\omega^2/g+k\tanh(kd)}\frac{\cosh(k(z+d))}{\cosh(kd)}e^{i(kx+\omega t)}\mathrm{d}k\mathrm{d}\omega, \tag{15}$$

where $\hat{\mathcal{F}}^{(-2)}_\mathrm{I,R}=\int_{-\infty}^{\infty}\int_{-\infty}^{\infty}\mathcal{F}^{(-2)}_\mathrm{I,R}\exp(-i(kx+\omega t))\mathrm{d}x\mathrm{d}t$ is the Fourier transform of $\mathcal{F}^{(-2)}_\mathrm{I,R}$.

2.3.2. Surface elevation and run-up

Starting with the super-harmonic terms, after substitution of the first-order solutions from Table 1 and the super-harmonic self-interaction potential (11) into (6), we readily obtain the well-known result for the surface elevation arising from self-interaction (e.g., Mei, 1989):

$$\eta_{\mathrm{I}}^{(+2)} = \frac{k_0 \cosh(k_0 d)}{4 \sinh^3(k_0 d)} \left(2\cosh^2(k_0 d) + 1\right) A_{\mathrm{I}}^2 \cos(2\varphi_{\mathrm{I}}), \tag{16}$$

which simply corresponds to the super-harmonic term for a regular Stokes wave modulated by an envelope $A_{\mathrm{I}}(X_{\mathrm{I}})$, and similarly for the reflected wave (upon replacement of I by R in (16)).

By substituting the first-order solutions from Table 1 and the super-harmonic cross-interaction potential (12), we can show the surface elevation arising from cross-interaction is zero:

$$\eta_{\mathrm{I,R}}^{(+2)} = 0. \tag{17}$$

which is consistent with the deep-water limit in McAllister et al. (2018) and McAllister and van den Bremer (2019).

Turning to the sub-harmonic terms, by substituting the first-order solutions from Table 1 and the sub-harmonic self-interaction potential from (13) into (5), we recover from the self-interaction terms the well-known set-down (Mei, 1989; Longuet-Higgins and Stewart, 1962)

$$\eta_{\mathrm{I}}^{(-2)} = -\frac{g|A_{\mathrm{I}}|^2}{2(gd - c_{g,0}^2)} \left[\frac{2c_{g,0}}{c_{p,0}} - \frac{1}{2}\right], \tag{18}$$

where we have additionally made the commonly made shallow-return flow assumption (see Calvert et al., 2019).

For the sub-harmonic cross-interaction potential (15) the shallow-return flow assumption cannot be made, as the forcing $\mathcal{F}_{\mathrm{I,R}}$ given in (14) also includes rapidly varying terms in x, which require a non-shallow depth dependence to satisfy Laplace. We therefore obtain a solution in the form of a bivariate inverse Fourier transform:

$$\begin{aligned}\eta_{\mathrm{I,R}}^{(-2)} &= \frac{1}{2}\left(\tanh(k_0 d) + \frac{1}{\tanh(k_0 d)}\right) k_0 A_{\mathrm{I}} A_{\mathrm{R}} \cos(\varphi_{\mathrm{I}} - \varphi_{\mathrm{R}}) \\ &\quad - \frac{1}{g}\int_{-\infty}^{\infty}\int_{-\infty}^{\infty} \frac{i\omega \hat{F}_{\mathrm{I,R}}^{(-2)}}{-\omega^2/g + k\tanh(kd)} e^{i(kx+\omega t)} \mathrm{d}k\mathrm{d}\omega,\end{aligned} \tag{19}$$

which cannot be evaluated in closed form. However, the integral term in (19) evaluates to zero at $x = x_{\mathrm{w}}$, as can be shown numerically by increasing the resolution of the Fourier transform.

The total second-order run-up at the wall can now be calculated by summing (16)–(19), including self-interacting terms for both incident and reflected groups, and evaluating the result at the wall $x = x_{\mathrm{w}}$. Fig. 1 gives the non-dimensional contributions to run-up from the self-interacting and cross-interacting terms as a function of relative water depth $k_0 d$. All of the second-order contributions increase in magnitude with shallower water depth. Fig. 1a gives the contributions of the super-harmonic terms. As derived, the cross-interaction term is zero, and thus the total super-harmonic run-up is twice the self-interaction term present in the absence of a wall. Fig. 1b shows the sub-harmonic run-up contributions. The cross-interaction term is shown to give a positive contribution, opposite to the normal set-down under wavepackets. Note that this term is modulated by a standing-wave pattern that varies rapidly in space. This set-up is equivalent to that derived for crossing seas in deep water by McAllister et al. (2018). In shallower depth the total sub-harmonic run-up is thus negative, whereas in deep water the positive set-up dominates, and the total sub-harmonic run-up becomes positive. Fig. 1c compares the magnitude of the total second-order sub- and super-harmonic run-up at the wall. Note that the temporal structure of each is very different, with the super-harmonic run-up oscillating at twice the carrier frequency whilst the sub-harmonic run-up changes slowly in time on the group scale.

2.3.3. Force on a vertical wall

The force on a vertical wall is obtained from vertically integrating pressure. At second order, the force is comprised of three terms,

$$F^{(2)}/b = +\int_0^{\eta^{(1)}} p^{(0)}\mathrm{d}z + \int_0^{\eta^{(1)}} p^{(1)}\mathrm{d}z + \int_{-d}^{0} p^{(2)}\mathrm{d}z, \tag{20}$$

where b is the width of the vertical wall, and the hydrostatic pressure $p^{(0)}$ only has to be integrated up to $\eta^{(1)}$, as including $\eta^{(2)}$ would include higher-order terms that are ignored. Below, we will consider the three contributions to (20) in turn, before considering sub-harmonic ($F^{(-2)}$) and super-harmonic ($F^{(+2)}$) force contributions individually. Throughout this section, we will use the shorthand $C \equiv \cos$.

First, integration of the zeroth-order (or hydrostatic) pressure up to the first-order free-surface elevation gives,

$$\begin{aligned}\int_0^{\eta^{(1)}} p^{(0)}\mathrm{d}z &= -\frac{\rho g}{4}\left[A_{\mathrm{I}}^2(1 + C(2\varphi_{\mathrm{I}})) + A_{\mathrm{R}}^2(1 + C(2\varphi_{\mathrm{R}}))\right. \\ &\quad \left. + 2A_{\mathrm{I}}A_{\mathrm{R}}(C(\varphi_{\mathrm{I}} - \varphi_{\mathrm{R}})) + C(\varphi_{\mathrm{I}} + \varphi_{\mathrm{R}})\right], \\ &= -\rho g A_{\mathrm{w}}^2\left[1 + C(2\varphi_{\mathrm{w}})\right],\end{aligned} \tag{21}$$

where the second identity evaluates the force contribution on the wall ($x = x_{\mathrm{w}}$), with $\varphi_{\mathrm{w}} = -\omega_0 t + \mu_{\mathrm{I}}$ and $A_{\mathrm{w}}(t) = A_{\mathrm{I}}(x = x_{\mathrm{w}}, t)$.

Second, integration of the first-order pressure up to the first-order free-surface elevation gives,

$$\begin{aligned}\int_0^{\eta^{(1)}} p^{(1)}\mathrm{d}z &= \frac{\rho g}{2}\left[A_{\mathrm{I}}^2(1 + C(2\varphi_{\mathrm{I}})) + A_{\mathrm{R}}^2(1 + C(2\varphi_{\mathrm{R}}))\right. \\ &\quad \left. + 2A_{\mathrm{I}}A_{\mathrm{R}}(C(\varphi_{\mathrm{I}} - \varphi_{\mathrm{R}})) + C(\varphi_{\mathrm{I}} + \varphi_{\mathrm{R}})\right], \\ &= 2\rho g A_{\mathrm{w}}^2\left[1 + C(2\varphi_{\mathrm{w}})\right],\end{aligned} \tag{22}$$

where the second identity again evaluates the force contribution on the wall ($x = x_{\mathrm{w}}$).

From (7), the second-order pressure is given by $p^{(2)} = -\rho\left(\partial_t\phi^{(2)} + \frac{1}{2}|\nabla\phi^{(1)}|^2\right)$. The second term in $p^{(2)}$ gives for the second-order contribution to force:

$$\begin{aligned}&\int_{-d}^{0} -\rho\frac{1}{2}|\nabla\phi^{(1)}|^2\mathrm{d}z = -\frac{\rho g}{\sinh(2k_0 d)}\Big\{ \\ &\frac{1}{2}\left[A_{\mathrm{I}}^2\left(1 + C(2\varphi_{\mathrm{I}})\right) + A_{\mathrm{R}}^2\left(1 + C(2\varphi_{\mathrm{R}})\right)\right]\left(\frac{k_0 d}{2} + \frac{\sinh(2k_0 d)}{4}\right) \\ &+ \frac{1}{2}\left[A_{\mathrm{I}}^2\left(1 - C(2\varphi_{\mathrm{I}})\right) + A_{\mathrm{R}}^2\left(1 - C(2\varphi_{\mathrm{R}})\right)\right]\left(-\frac{k_0 d}{2} + \frac{\sinh(2k_0 d)}{4}\right) \\ &- 2A_{\mathrm{I}}A_{\mathrm{R}}\left[C(\varphi_{\mathrm{I}} - \varphi_{\mathrm{R}})k_0 d + C(\varphi_{\mathrm{I}} + \varphi_{\mathrm{R}})\frac{\sinh(2k_0 d)}{2}\right]\Big\}, \\ &= \rho g A_{\mathrm{w}}^2\left\{\left(-\frac{1}{2} + \frac{2k_0 d}{\sinh(2k_0 d)}\right) + \left(-\frac{k_0 d}{\sinh(2k_0 d)} + 1\right)C(2\varphi_{\mathrm{w}})\right\},\end{aligned} \tag{23}$$

where the second identity again evaluates the force contribution on the wall ($x = x_{\mathrm{w}}$). The first term in $p^{(2)}$ has the super-harmonic term (from depth-integrating the time-derivative of the corresponding potentials):

$$\begin{aligned}&\int_{-d}^{0} -\rho\partial_t\phi^{(+2)}\mathrm{d}z = \rho g\left\{\frac{3}{4\sinh^2(k_0 d)}\left(A_{\mathrm{I}}^2 C(2\varphi_{\mathrm{I}}) + A_{\mathrm{R}}^2 C(2\varphi_{\mathrm{R}})\right)\right. \\ &\left. - \frac{k_0 d\tanh(k_0 d)}{2}\left(3 + \frac{1}{\tanh^2(k_0 d)}\right)A_{\mathrm{I}}A_{\mathrm{R}}C(\varphi_{\mathrm{I}} + \varphi_{\mathrm{R}})\right\}, \\ &= \rho g A_{\mathrm{w}}^2\left\{\frac{3}{2\sinh^2(k_0 d)} - \frac{k_0 d\tanh(k_0 d)}{2}\left(3 + \frac{1}{\tanh^2(k_0 d)}\right)\right\}C(2\varphi_{\mathrm{w}}),\end{aligned} \tag{24}$$

and the sub-harmonic term:

$$\begin{aligned}&\int_{-d}^{0} -\rho\partial_t\phi^{(-2)}\mathrm{d}z \\ &= -\frac{\rho\omega_0 c_{g,0}}{2(1 - c_{g,0}^2/(gd))\tanh(k_0 d)}\left(1 + \frac{c_{g,0}\omega_0}{g\sinh(2k_0 d)}\right)(A_{\mathrm{I}}^2 + A_{\mathrm{R}}^2) \\ &- \rho\frac{1}{4\pi^2}\int_{-\infty}^{\infty}\int_{-\infty}^{\infty}\frac{i\omega\hat{F}_{\mathrm{I,R}}^{(-2)}}{-\omega^2/g + k\tanh(kd)}\frac{\tanh(kd)}{k}e^{i(kx+\omega t)}\mathrm{d}k\mathrm{d}\omega,\end{aligned} \tag{25}$$

where the second identity in (24) again evaluates the force contribution on the wall ($x = x_{\mathrm{w}}$). In (25), we have applied the shallow-return

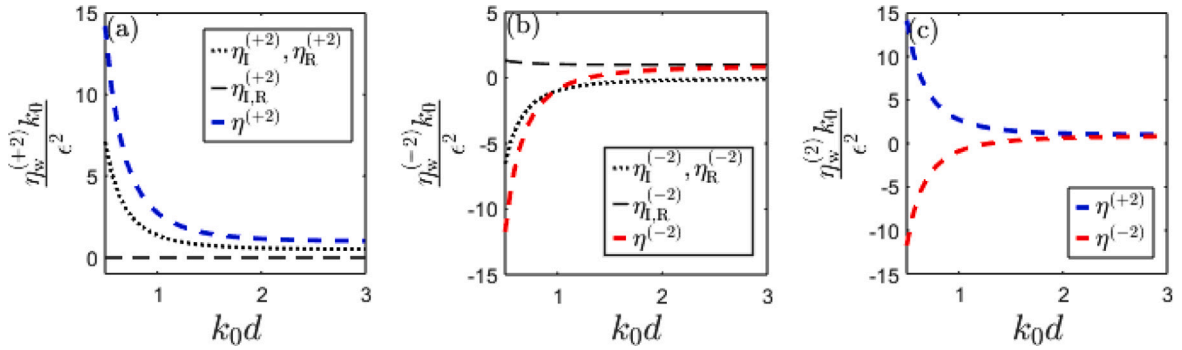

Fig. 1. Non-dimensional contributions to run-up from second-order self $\eta_{\mathrm{I}}^{(\pm 2)}$ and cross $\eta_{\mathrm{I,R}}^{(\pm 2)}$ interaction terms as well as their combined contribution for: (a) super-harmonic, (b) sub-harmonic, and (c) comparison of the total second-order contributions of both sub- and super-harmonics. Note these values are taken when the centre of the group is at the wall to show either a maximum or minimum.

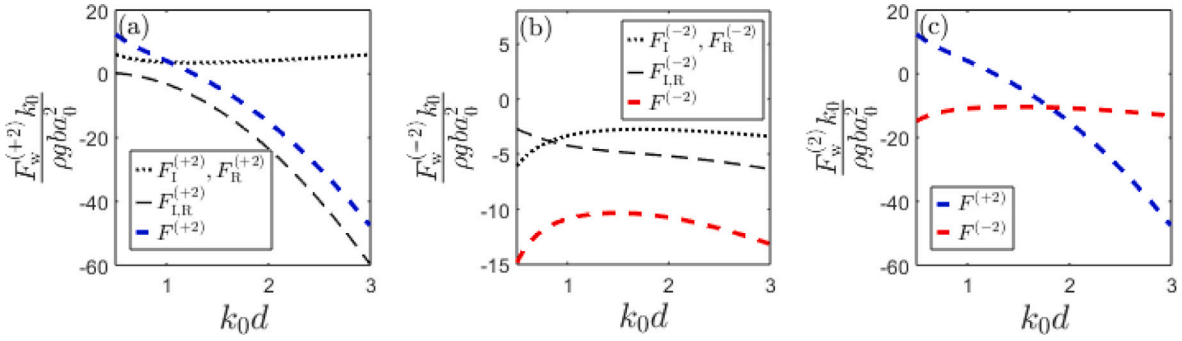

Fig. 2. Non-dimensional contributions to force on the vertical wall from second-order terms. (a) Super-harmonic, (b) sub-harmonic, and (c) total second-order contribution. Note, these values are taken when the centre of the group is at the wall to show either a maximum or minimum.

flow assumption (see, e.g., Calvert et al., 2019) to simplify the self-interaction terms but not the cross-interaction terms. Similar to the sub-harmonic surface elevation, the integral term in (25) and in (19) evaluates to zero at $x = x_{\mathrm{w}}$, as can be shown numerically by increasing the resolution of the Fourier transform.

Combining the contributions in (21)–(25), the total second-order force on the wall is given as the super-harmonic part,

$$F_{\mathrm{w}}^{(+2)} = \rho g b A_{\mathrm{w}}^2 \Bigg\{ \underbrace{\frac{1}{2} - \frac{k_0 d}{\sinh(2k_0 d)} + \frac{3}{2\sinh^2(k_0 d)}}_{\text{Self-interaction terms}} + \underbrace{\frac{3}{2} - \left(3 + \frac{1}{\tanh^2(k_0 d)}\right) \frac{k_0 d \tanh(k_0 d)}{2}}_{\text{Cross-interaction terms}} \Bigg\} \cos(2\varphi_{\mathrm{w}}), \tag{26}$$

and the sub-harmonic part,

$$F_{\mathrm{w}}^{(-2)} = \rho g b A_{\mathrm{w}}^2 \Bigg[\underbrace{-\frac{\omega_0 c_{g,0}}{g(1 - c_{g,0}^2/(gd))\tanh(k_0 d)} \left(1 + \frac{c_{g,0}\omega_0}{g\sinh(2k_0 d)}\right)}_{\text{Self-interaction terms}} + \underbrace{\frac{1}{2} + \frac{2k_0 d}{\sinh(2k_0 d)}}_{\text{Cross-interaction term}} \Bigg] \underbrace{- \rho \frac{1}{4\pi^2} \int_{-\infty}^{\infty} \int_{-\infty}^{\infty} \frac{i\omega \hat{F}_{\mathrm{I,R}}^{(-2)}}{-\omega^2/g + k\tanh(kd)} \frac{\tanh(kd)}{k} e^{i(kx_{\mathrm{w}} + \omega t)} \mathrm{d}k\mathrm{d}\omega}_{\text{Cross-interaction term}}, \tag{27}$$

where as before $\varphi_{\mathrm{w}} = -\omega_0 t + \mu_{\mathrm{I}}$ and $A_{\mathrm{w}}(t) = A_{\mathrm{I}}(x = x_{\mathrm{w}}, t)$, and the integral term evaluates to zero and is only included for completeness.

Fig. 2 gives the non-dimensional contributions of self and cross-interaction terms to force on the vertical wall as a function of $k_0 d$. In which, a_0 is the offshore amplitude of the first-order wave group. Fig. 2a provides the contributions for the super-harmonic part, Fig. 2b for the sub-harmonic part and Fig. 2c compares the total second-order harmonic contributions of sub- and super-harmonics.

2.4. Sub-harmonic error wave

When first-order generation is used, a sub-harmonic error wave is unintentionally formed as compensation for the volume of fluid that is normally contained in the set-down, which is not created by the wavemaker. Due to its low frequency, the sub-harmonic error wave travels ahead of the wave group in the flume. We can provide an estimate of the error wave by inverting the set-down of the wavepacket, which is created at the wavemaker and letting this travel ahead at the shallow-water wave speed $\sqrt{gd}$:

$$\eta_{\mathrm{ew}} = \frac{g A_{\mathrm{I}}^2 (x - \sqrt{gd}t)}{2(gd - c_{g,0}^2)} \left(\frac{2c_{g,0}}{c_{p,0}} - \frac{1}{2}\right). \tag{28}$$

The corresponding force (per unit width) for this shallow-water wave can be computed according to linear wave theory:

$$F_{\mathrm{w,ew}}/b = 2\rho g d \eta_{\mathrm{ew}}(x = x_{\mathrm{w}}). \tag{29}$$

3. Experimental methodology

3.1. Experiment set-up

The experiments are carried out in a wave flume of 20 m length, 0.6 m width and 0.25 m water depth, located in the COAST (Coastal, Ocean And Sediment Transport) Laboratory, at the University of Plymouth, UK. The experimental set-up is illustrated in Fig. 3. Wave generation is provided by a piston-type wavemaker, designed and built by Edinburgh Designs Ltd with an elongated paddle displacement range for implementation of second-order wave generation (outlined by Mortimer et al., 2022). The paddle resting position is at $x = 0$ m,

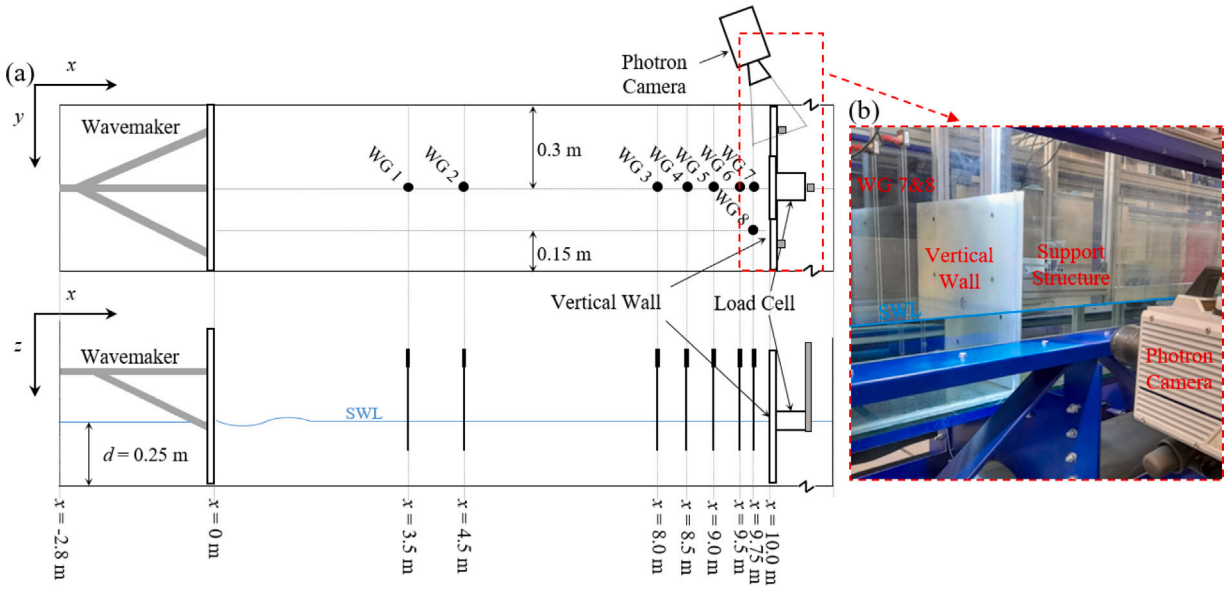

Fig. 3. The experimental set-up: (a) a schematic representation of the set-up, showing wave gauge locations (WG 1:8), vertical wall, Photron camera and load cell within the flume; (b) a photograph of the vertical wall and Photron camera set-up.

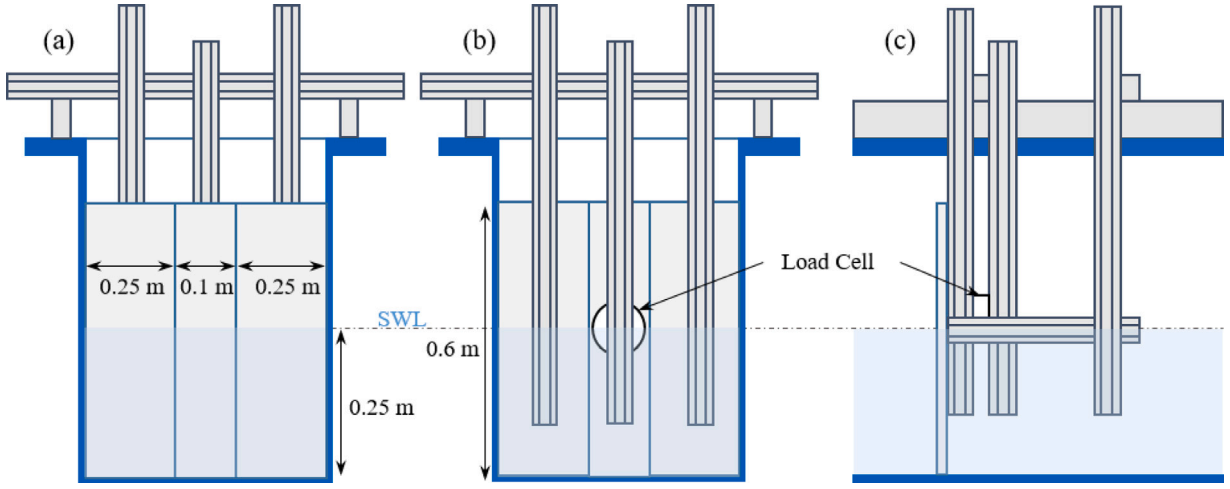

Fig. 4. Schematic representation of the vertical wall construction: (a) front view, (b) rear view, (c) cross-sectional side view.

from where all locations are referenced. The vertical wall location is at $x = x_w = 10$ m. Eight resistive-type wave gauges (WG 1:8) measure the free-surface elevation at 128 Hz. WG 1:7 are aligned along the central-line of the flume, and WG 8 is mounted at the mid-point between WG 7 and the flume side wall at $x = 9.75$ m, in order to monitor the lateral structure of the wave field.

A single-axis load cell, mounted on an aluminium beam support structure, is used to determine the dynamic horizontal wave force on the vertical wall. A schematic sectional view of the vertical wall construction is shown in Fig. 4. It comprises three horizontal panels of 18 mm thick rigid PVC sheet. The two side panels are mounted directly onto the rigid support structure and sealed to the flume walls. The central panel of 0.1 m width is attached to the load cell, which is then mounted to the support structure at the still water level. The different panels reduce the force from the full 0.6 m wall width going through the load cell so that the instrument is kept within its operational limit. Between the three panels are 1 mm gaps, to ensure the force measurements on the central panel is unconstrained. These gaps are covered with flexible plastic film to prevent unwanted flow through the wall. Only the dynamic load, excluding hydrostatic force, is measured on the vertical wall, as the set-up is wet-back, with the still water level equal in front and behind. The horizontal displacement of the vertical wall is sufficiently small that we can ignore the dynamic response of the water behind the wall when wave impact on the front of the wall occurs. Fig. 5 is a photograph of a wave group interacting with the vertical wall. Finally, a settling period of 10 min between experiments allows seiche effects to dissipate.

3.1.1. Video recording of wave run-up

Building on the method established by Dassanayake et al. (2019) and Antonini et al. (2021) in the COAST laboratory, wave run-up on the vertical wall was recorded with a Photon ultra slow-motion camera at 400 fps. The camera focused on the vertical wall at an approximate 15° angle, where the closest edge of the wall was the focal point. An LED lamp highlighted the water surface in the recorded greyscale images. To limit unnecessarily large volumes of data, only 10 s of video around the predicted time of the wave group-wall interaction was recorded. A chequered calibration board enabled the focused frame to be calibrated. Calibration involved removal of the intrinsic distortion of the images and extrinsic rotation of the oblique focal plane, to allow

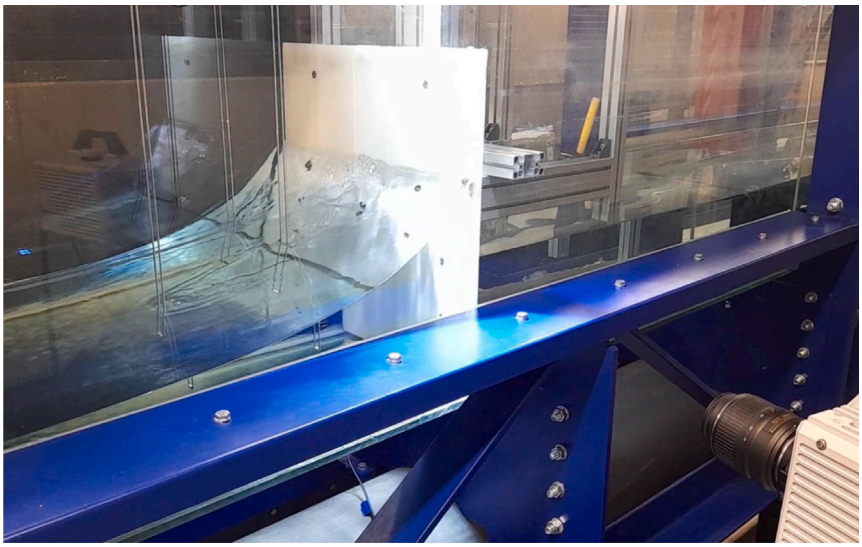

Fig. 5. Photograph capturing the central wave crest of a group impacting the vertical wall. The Photron slow-motion camera is seen in the bottom right.

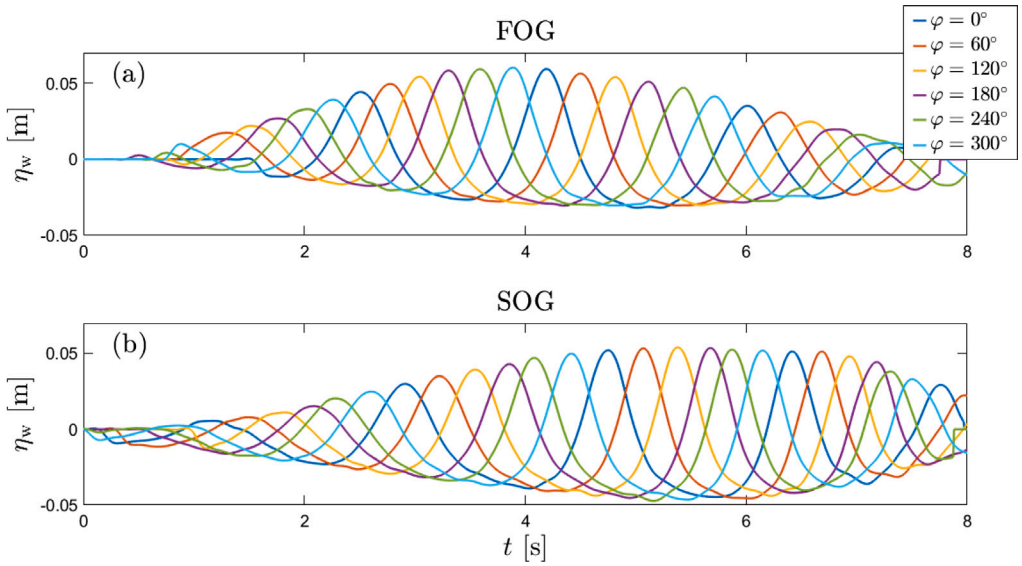

Fig. 6. Measured run-up time series for experiment 2. (a) First-order generated wave field run-up, (b) second-order generated wave field run-up.

accurate run-up distances to be determined. The run-up time series was obtained through a manual tracking procedure in MATLAB, which involved clicking on the maximum extent of run-up in each recorded image.

3.2. Experimental matrix

Table 2 shows the experimental matrix of sixteen wave group parameters. Consistent with the work presented by Mortimer et al. (2022), the wave groups were designed to have a Gaussian shape in space and time. The Gaussian wave packets used are expressed as

$$A = a_0 \exp\left(-\frac{\left((x - x_f) - c_{g,0}(t - t_f)\right)^2}{2\sigma^2}\right), \tag{30}$$

where σ is the characteristic length scale of the wave group, and x_f and t_f are the location and time of focus, respectively. Although our theory is narrow-banded and thus does not include the effects of linear focusing, we use broad-banded linear dispersive theory to generate the linear part of the wave signal.

Three non-dimensional numbers characterise each experiment: the non-dimensional water depth $k_0 d$; the steepness $\epsilon = k_0 a_0$; and the bandwidth $\nu = \sqrt{m_2 m_0 / m_1^2 - 1}$, where m_n is the nth moment of the energy spectrum. For Gaussian groups, the energy spectrum $S(\omega)$ of the surface elevation can be readily evaluated in closed form as

$$S = \frac{\sigma^2 a_0^2}{4\sqrt{\pi} c_{g,0}} \exp\left(-\frac{(\omega - \omega_0)^2 \sigma^2}{4 c_{g,0}^2}\right), \tag{31}$$

from which the bandwidth parameter ν is obtained: $\nu = \sqrt{2} c_{g,0}/(\sigma\omega_0) = \sqrt{2} n/(k_0\sigma)$ with $n = c_{g,0}/c_{p,0} = 1/2\left(1 + 2k_0 d/\sinh(2k_0 d)\right)$. Each experiment was repeated with six different phase shifts defined as the relative phase of the carrier wave at the focus location $\mu = [0, 60, 120, 180, 240, 300°]$, and each phase variation was generated twice, once using

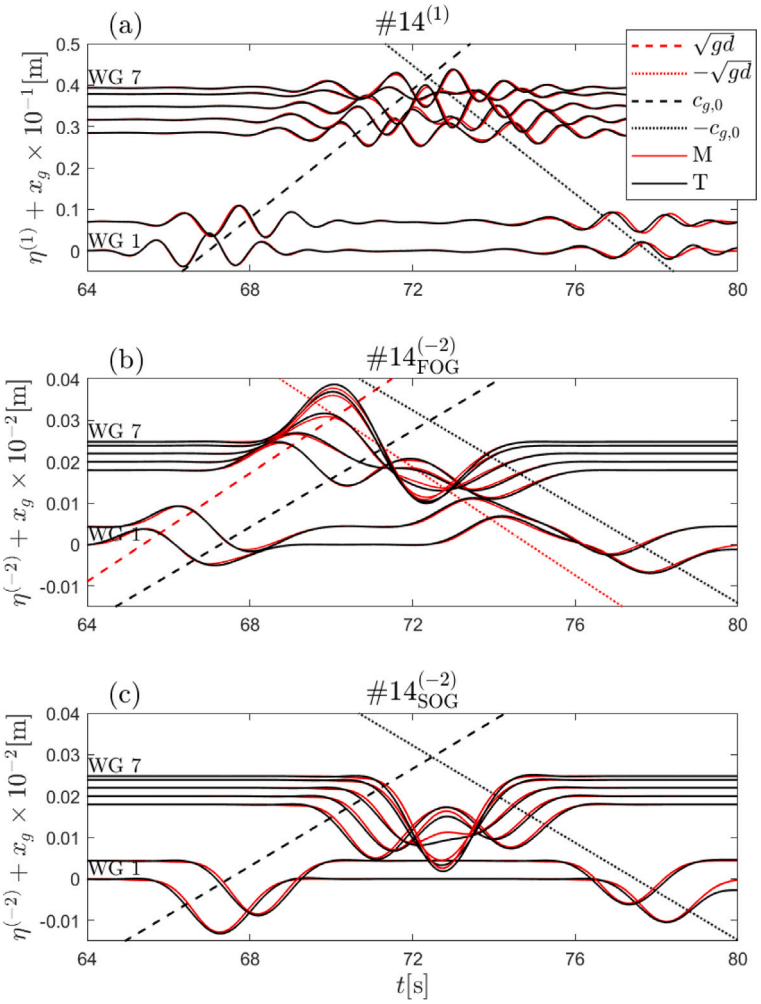

Fig. 7. Measured (M) and theoretical (T) free surface at WG 1:7 with vertical offset by gauge location x_g: (a) first-order free surface, (b) first-order generated sub-harmonic free surface, (c) second-order generated sub-harmonic free surface. First-order group speed is indicated with a dashed black line and shallow-water wave speed is indicated with dashed red lines. Reflected speeds are indicated with dotted lines.

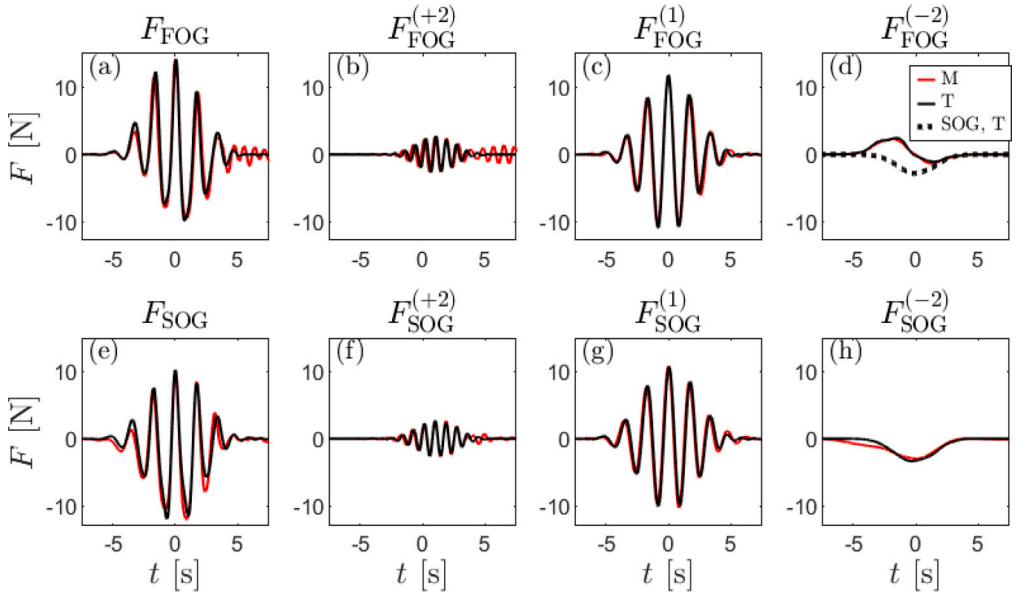

Fig. 8. Experiment #2 measured (M) and theoretical (T) dynamic force time series for first-order generation (FOG) and second-order generation (SOG). (a) and (e) total dynamic force, (b) and (f) super-harmonic contributions, (c) and (g) linear contributions, (d) and (h) sub-harmonic contributions.

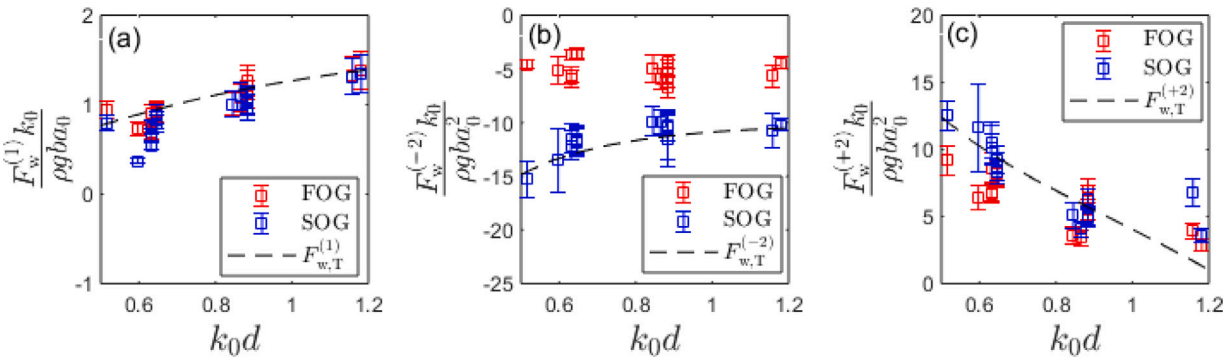

Fig. 9. Maximum non-dimensional dynamic force as a function of $k_0 d$ when the centre of the group is at the wall. (a) Linear force, (b) second-order sub-harmonic force, and (c) second-order super-harmonic force.

Table 2
Experimental matrix.

Experiment	f_0 [Hz]	$\epsilon = k_0 a_0$	ν	$k_0 d$	$c_{g,0}$ [m/s]	$\Delta X^{(-2)}_{p,\text{total}}$ [m]
1	0.49	0.08	0.19	0.50	1.36	−0.47
2	0.61	0.09	0.19	0.63	1.28	−0.21
3	0.61	0.12	0.19	0.63	1.28	−0.38
4	0.61	0.14	0.19	0.63	1.28	−0.52
5	0.60	0.15	0.19	0.61	1.29	−0.67
6	0.60	0.12	0.37	0.61	1.29	−0.26
7	0.60	0.15	0.37	0.61	1.29	−0.41
8	0.60	0.20	0.36	0.60	1.31	−0.81
9	0.79	0.23	0.17	0.86	1.13	−0.35
10	0.79	0.25	0.17	0.86	1.13	−0.41
11	0.79	0.27	0.17	0.86	1.13	−0.48
12	0.79	0.29	0.17	0.86	1.13	−0.55
13	0.78	0.09	0.28	0.84	1.14	−0.04
14	0.77	0.25	0.33	0.83	1.15	−0.29
15	0.99	0.25	0.15	1.15	0.95	−0.11
16	0.98	0.40	0.15	1.14	0.96	−0.32

first-order paddle displacement $X_p^{(1)}$ and again with the additional second-order correction $X_p^{(2)}$ applied. Four peak frequencies were selected $(0.5, 0.6, 0.8, 1.0)$ Hz to correspond to relative depths of $k_0 d = 0.5, 0.6, 0.9, 1.1$. The bandwidths were chosen so that the groups remained quasi-monochromatic, but sufficiently compact in time and space for sub-harmonic error waves, which are present in the first-order generated experimental cases, to partially separate out ahead of the first-order group, due to their difference in celerity (see Mortimer et al., 2022). Each experiment had a duration of $T = 128$ s, and a wave group focus location and time of $x_f = 10$ m and $t_f = T/2$, respectively. Finally, in the right hand column of Table 2 is the required sub-harmonic net-backwards displacement of the wavemaker in order to compensate for sub-harmonic error waves present for each case at its respective relative depth $k_0 d$. The paddle displacement formulation is derived by Van Leeuwen and Klopman (1996) and outlined in full by Mortimer et al. (2022).

3.3. Harmonic separation

In order to predict the run-up and force on the vertical wall using the theory developed in Section 2, deconstruction of the measured free surface into different orders in steepness is required. This section outlines the procedure we used to isolate harmonic contributions to the wave field at WG 1, the furthest wave gauge from x_w, to minimise the effect of reflections and non-zero terms near the wall. We use a two-phase harmonic extraction (or phase inversion) technique outlined by Baldock et al. (1996), Hunt (2003) and Mortimer et al. (2022). The six phase variations of our experimental cases give three combinations of groups, inverted by 180°. Combination of the inverted time series yields the odd or even orders in steepness respectively,

$$\eta_{\text{odd}} = \frac{\eta_0 - \eta_{180}}{2} \quad \text{and} \quad \eta_{\text{even}} = \frac{\eta_0 + \eta_{180}}{2}, \tag{32a,b}$$

where η_0 and η_{180} denote a crest- and trough-focused wave group, respectively. At the leading order, η_{odd} is dominated by the first-order signal, and η_{even} by the second-order signal for an underlying Stokes expansion. The latter comprises bound waves, which are predominantly the bound set-down and possibly free error waves in the case of first-order generation. The free surfaces of each harmonic component are revealed with judicious filtering of the η_{odd} and η_{even} terms. Filtering at $0.5f_0 - 1.5f_0$ yields the first-order contribution; $< 0.5f_0$ yields the sub-harmonic contribution and $1.5f_0 - 2.5f_0$ yields the super-harmonic contribution. In addition to free-surface measurements, we have applied the same harmonic isolation method to force and run-up measurements.

Consistent with Section 2, we denote run-up as η_w, using the subscript notation for measured (M) and theoretical (T) results. Fig. 6 shows run-up time series for all six phase variations of experiment #2. The figure shows run-up associated with first-order generation (FOG) in Fig. 6a and second-order generation (SOG) in Fig. 6b. All experimental group cases are intentionally kept beneath the breaking limit, and therefore the run-up of all six phase variations of each case fit within an envelope. This is important to note as the phase of the incident wave group only changes the relative position of the run-up within the bounds of an envelope. Therefore, for non-breaking cases, the maximum of the envelope gives the greatest possible run-up, which is the parameter of most interest in for the present work. The same phase variation, bound within an envelope, is seen for the force measurements, and so the same method is used.

Repeatability of the experimental cases is assessed from the six phase variations of each wave group case. This is achieved through isolation of the first-order wave group contribution to free surface, force and run-up. The envelope of the first-order contribution is given by the absolute of a Hilbert transform of the first-order time series. Repeatability is then examined in the results section by including error bars (shown later in the paper) indicating two standard deviations around the mean obtained from the six phase repeats. This method is only applicable in this instance as the wave group cases are non-breaking.

Finally, visual quality control (described in Appendix A) was applied to all time series before the maximum theoretical force and run-up of each case is calculated as the summation of the maximum of the first-order contribution envelope and the phase-independent super-harmonic and sub-harmonic contributions, where the first-order and second-order sub- and super-harmonic contributions are appropriately shifted in time before the summation, to account for the relative difference in speed. This theoretically predicted maximum gives the greatest run-up and force predictions, without the influence of first-order wave group phase.

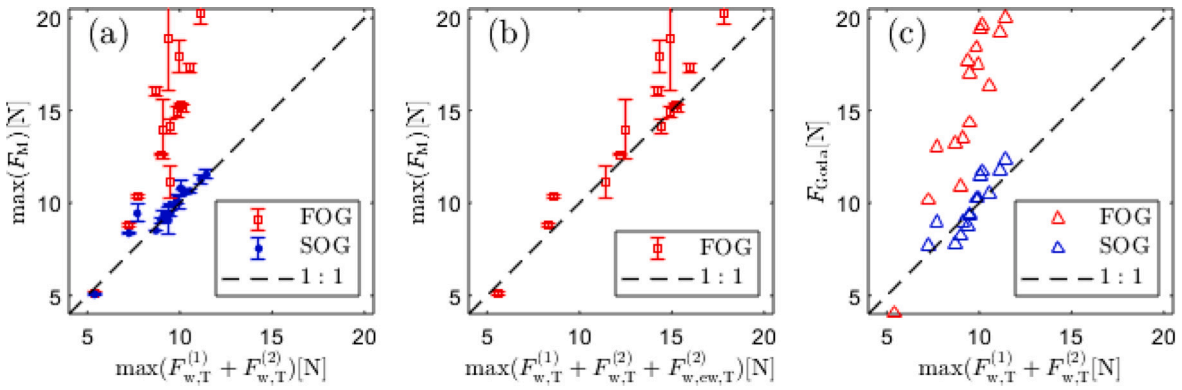

Fig. 10. Comparison between maximum measured and theoretical forces on a wall when first-order (F_{FOG}) or second-order wave generation (F_{SOG}) are used. The maximum of linear and super-harmonic envelopes have been used to avoid the effect of phase.

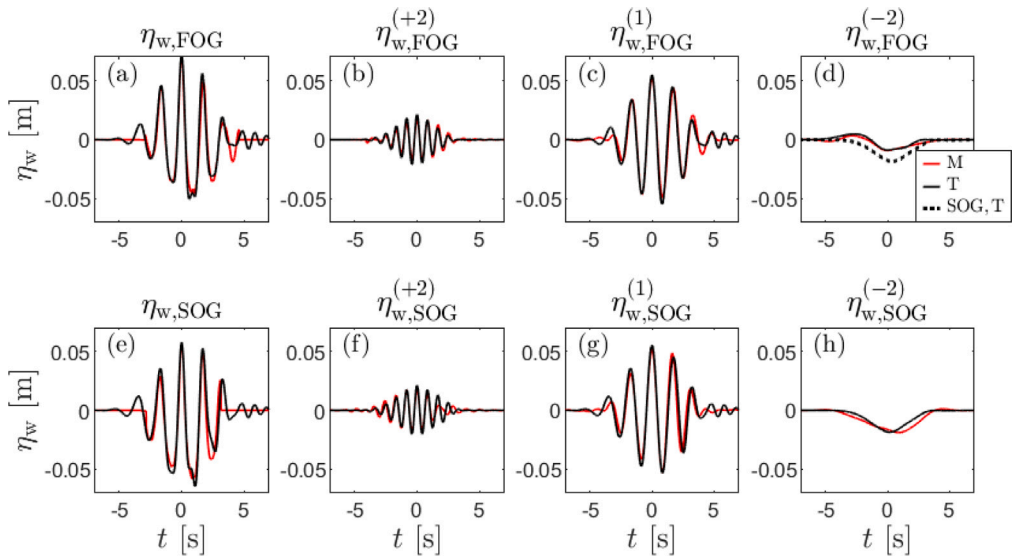

Fig. 11. Experiment #2 measured (M) and theoretical (T) run-up time series for first-order generation (FOG) and second-order generation (SOG). (a) and (e) total run-up, (b) and (f) super-harmonic contributions, (c) and (g) linear contributions, (d) and (h) sub-harmonic contributions.

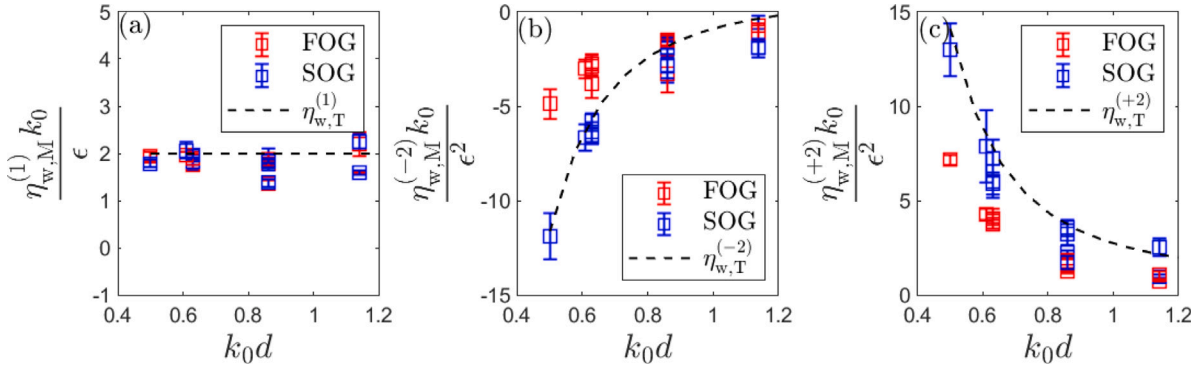

Fig. 12. Non-dimensional run-up as a function of $k_0 d$ evaluated when the centre of the group is at the wall, using the envelopes of linear and super-harmonic signals to avoid the effect of phase. (a) First-order run-up, (b) second-order sub-harmonic run-up, (c) second-order super-harmonic run-up.

4. Results

In this section we outline the results of our experimental campaign. First, we show the result of propagating the measured harmonic contributions at WG 1 throughout the flume to recreate the free surface, including reflections from the vertical wall. Following this, we outline the harmonic contributions to dynamic force and run-up measurements with time series of a particular experimental case before highlighting the force and run-up at the centre of the group for all cases compared with theory.

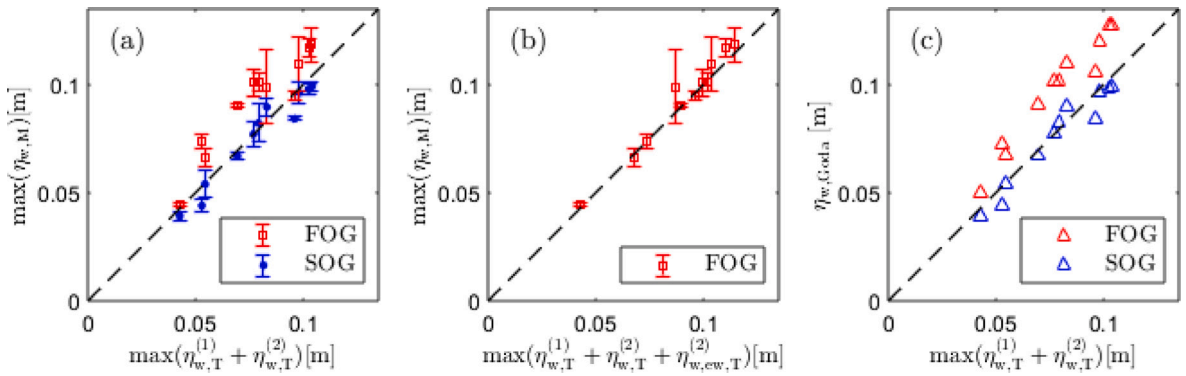

Fig. 13. Measured run-up vs theoretical run-up at the centre of the first-order wave group $t = 0$ s. Error bars are two standard deviations around mean of six phase repeats of each experiment. (a) for second-order generation (b) for first-order generation and (c) the predicted run-up from by Goda (1975) using first-order and second-order generated offshore wave conditions as input.

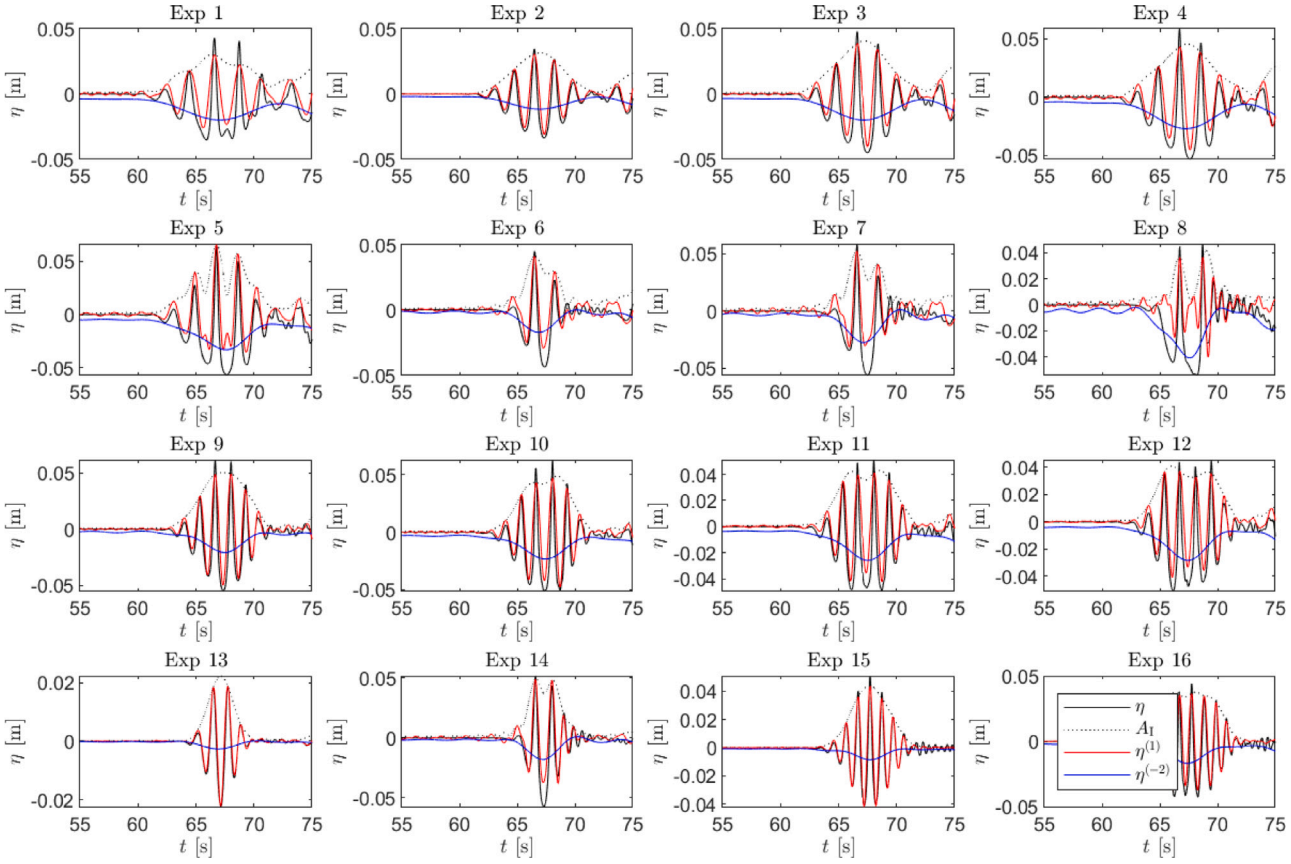

Fig. A.14. Raw time series of the free-surface elevation η for all experiments for the zero phase shift ($\varphi = 0°$). The window has been chosen to only show the incoming wave group before any reflections. The solid black line shows the raw signal at WG 1, the red line is the linear contribution, the dotted line is the envelope, and the blue solid line is the second-order sub-harmonic free surface.

4.1. Free surface

4.1.1. First-order group

The first-order free surface at all wave gauge locations within the flume can be recreated by propagating components, measured at WG 1, at their respective phase speed ($c_p = k/\omega$), given by the linear dispersion relation $\omega^2 = gk\tanh(kd)$. The component phases and amplitudes are given by a Fourier Transform of the measured first-order free-surface at WG 1. The sub-harmonic free surface is evaluated using (18) and (19) and the super-harmonic free-surface using (16) and (17). Fig. 7 compares the measured and theoretically derived free surfaces for experiment # 14 at WG 1:7. The time series at each gauge is vertically offset according to each gauge location x_g. Fig. 7a shows the first-order group and Fig. 7b and c show the second-order sub-harmonic terms resulting from first-order generation (FOG) and second-order generation (SOG), respectively. Complete reflection at the wall is shown to be a fair assumption, as the predicted and measured signals show close agreement. The first-order group speed ($\pm c_{g,0}$) is denoted as a diagonal black dashed line to indicate the expected location of the centre of the first-order group envelope.

4.1.2. Second-order sub-harmonic component

A theoretical sub-harmonic surface elevation is obtained as the sum of the theoretical set-down, given by (18) for both incoming and

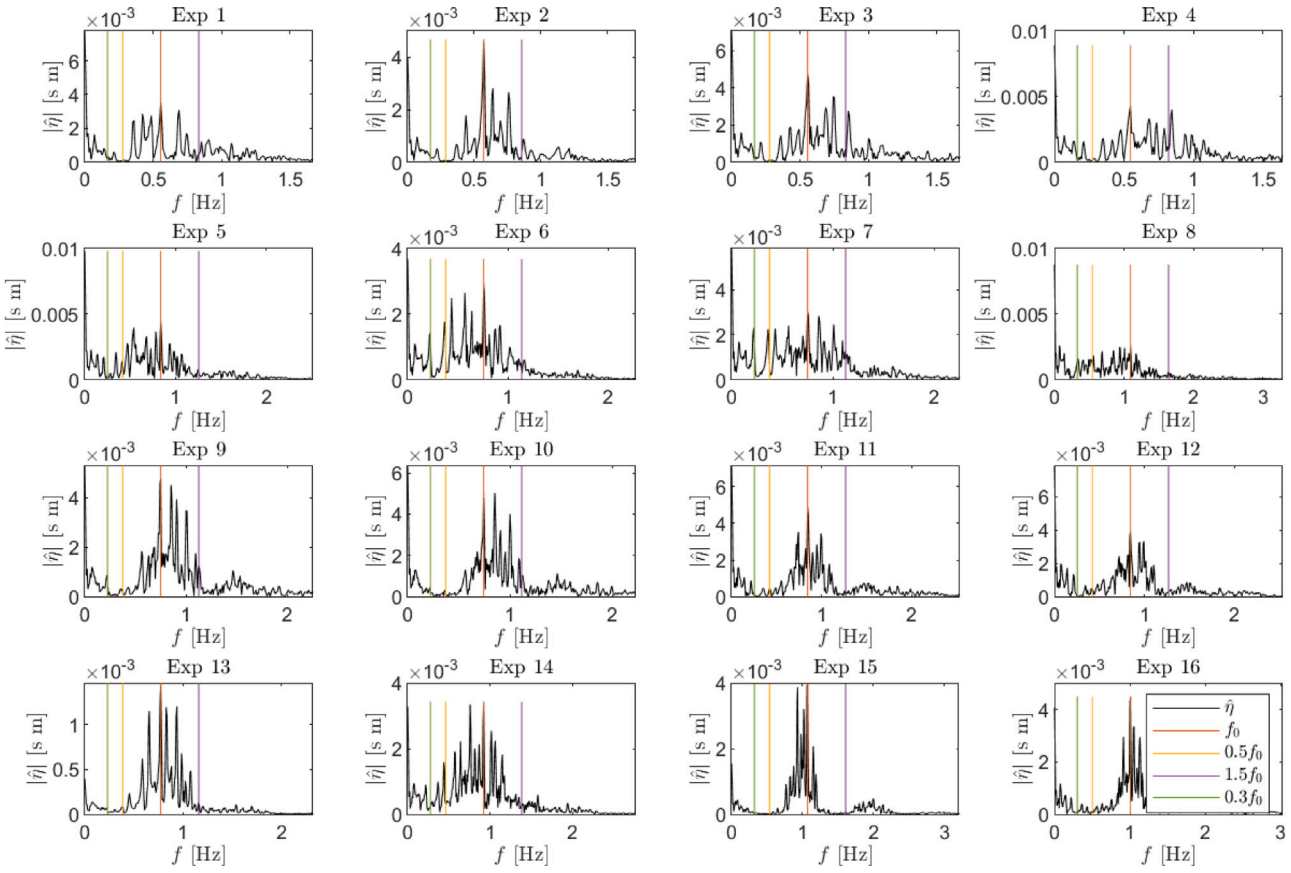

Fig. A.15. The magnitude of the Fourier transform of the raw time series of only the incoming wave group at wave gauge 1, shown with the black line. The coloured lines show the harmonic separation windows. The red line denotes f_0, found using the maximum of the spectrum, yellow to purple lines are the linear part and the green line is the sub-harmonic cut-off frequency.

reflected groups, which travels at the group speed $c_{g,0}$ and the interaction term (19). For first-order generated cases, the sub-harmonic error wave given by Eq. (28) is also included, which travels at the shallow-water speed $\sqrt{gd}$. Fig. 7b shows the measured (η_M) and theoretically reproduced (η_T) sub-harmonic free surface for case #14, where first-order wave generation is used, and therefore the error wave is present, seen as a crest at WG 1 at $t = 65$ s. Fig. 7c shows the second-order generated sub-harmonic free surface. The group speed $c_{g,0}$ is again denoted as a black line to indicate the centre of the sub-harmonic set-down and the shallow-water wave speed ($\sqrt{gd}$) is denoted as a red dashed line to indicate the relative position of the error wave. It is worth noting that the set-down given by the full second-order (broad-banded) theory, is given for all our experimental cases in Fig. C.18, included as an appendix.

4.2. Force measurements

Fig. 8 presents time series of force measurements from experiment #2, comparing measured and theoretical dynamic force on the wall from different harmonics, where the theoretical force is the sum of the first- and second-order harmonic contributions derived in Section 2, i.e., $F_T = F_T^{(1)} + F_T^{(-2)} + F_T^{(+2)}$. The maximum measured dynamic force, around $t = 0$ s of F_{FOG} and F_{SOG} show close agreement with the theoretically derived force. Fig. 8c and g plot the dynamic force associated with the linear wave fields. Here, the measured and theoretical predicted force show excellent agreement in amplitude and phase.

Fig. 8b and f show the measured super-harmonic force with the theoretical force, given by (26). Between $t = 3$ s and 7 s in Fig. 8b there is a super-harmonic force arising from an error wave, which appears to be mitigated with the second-order correction that has been applied in Fig. 8f. Fig. 8d and h show the measured sub-harmonic force, and the theoretically predicted force, given by (27). The theoretical second-order generated sub-harmonic force is shown as a dotted line in Fig. 8d, where the theoretical first-order generated (second-order) force (black solid line) has the addition of the error wave. When the theory accounts for the error wave force, there is good agreement with the measured sub-harmonic force (red line). The theoretical SOG force is shown as a black dashed line. The overall picture presented by Fig. 8 is that the significant difference in forces measured from first and second-order wave generated wave fields is due to force associated with the sub-harmonic error wave. The effect of the sub-harmonic error wave is highlighted in comparing the maximum force of Fig. 8a and e, which shows the maximum first-order generated wave force is 30% greater than the second-order generated wave force.

Fig. 9 plots non-dimensionalised measured force induced by first- (FOG) and second-order generated (SOG) wave groups as a function of relative depth $k_0 d$ for all 16 experimental cases. The mean of six phase repeats is plotted with the error bars indicating two standard deviations around the mean for each case. Each panel plots dynamic force associated with different group harmonics. The theoretically predicted force is indicated with a dashed black line. Fig. 9a presents the force associated with the first-order (linear) wave group, where as expected, both FOG and SOG groups are shown to induce a similar dynamic force on the vertical wall as there is no account for force associated with second-order harmonics. Both FOG and SOG show close agreement with the prediction. Fig. 9b presents the sub-harmonic force. Here, there is good agreement between the SOG force and the prediction. In all cases, FOG groups produce a larger force than both the SOG groups and the predictions; in shallower water depth, the difference between FOG and SOG groups increases. This is due to the presence of the

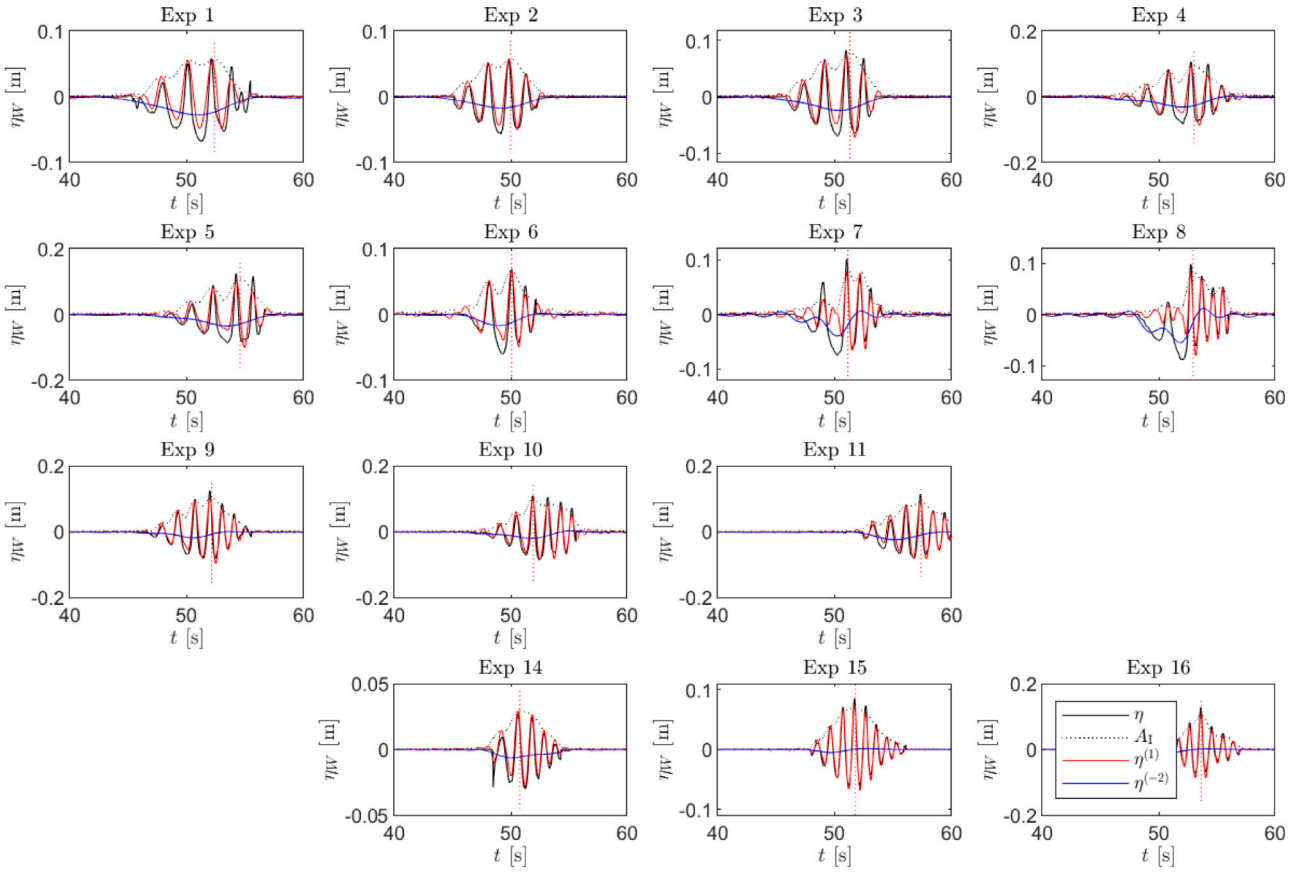

Fig. A.16. Raw time series of the run-up at the wall η_w for all experiments at zero phase shift. The solid black line shows the raw signal from camera processing, the red is then the linearised part with envelope in dotted black line and the blue solid line is the second-order sub-harmonic free surface. The dotted red lines shows the centre of the group. The raw signal has been padded with zeros before and after the ten second measured run-up time series.

sub-harmonic error wave which is greater in amplitude in shallower depths, has had less of an opportunity to separate from the first-order group, and therefore more superimposed upon the set-down associated with the main group, thus reducing the minimum force measurement. Fig. 9c presents the super-harmonic force from FOG and SOG groups, which increase as water depth reduces. Here, the SOG cases show better agreement with the prediction than the FOG cases. In the deepest cases, both SOG and FOG show poor agreement with the prediction, which is most likely due to these cases being the steepest and pushing the limit of the predictions, meaning that second-order prediction is not enough to recreate the measured signal.

Fig. 10 plots the maximum measured forces compared with the theoretically predicted forces from all 16 experimental cases. The mean of six phase variations of each case are shown with error bars indicating two standard deviations around the mean. In each panel the black dashed line shows a one to one agreement between predictions and measurements. Fig. 10a plots the maximum measured forces of first-order generated FOG and second-order generated SOG wave fields against the theoretical second-order generated force, which is composed of just the predicted first-order force and the force associated with the set-down. This plot indicates that the maximum predicted force for second-order generated cases are in close agreement with the second-order generated measurements, shown in blue. The first-order generated cases, shown in red, have the presence of the force associated with the sub-harmonic error wave, which shows an increase in the force measured over what is predicted. When the predicted force of the error wave is factored into the total force prediction, as is the case in Fig. 10b, it is seen that the predictions have better agreement with the first-order generated force measurements. There are still a few first-order generated force measurements which are greater than the predictions in Fig. 10b, specifically the steepest cases (#11, 12, 15 and 16), where higher-order non-linearities are more prevalent and the predictions begin to show limitations.

Fig. 10c plots the maximum dynamic wave force expected from the empirical formula derived by Goda (1975) (replicated in Appendix B for completeness) against the second-order predictions given by the theory derived herein. The plot shows a comparison between using the offshore wave condition of first-order generation, shown in red, and second-order generation, shown in blue, as an input for Goda's formula. It can be seen that the predicted force given by Goda is heavily dependent on the offshore wave condition used. When first-order wave generation is used without any second-order corrections, the force can be significantly over-predicted, up to 75% greater in the most extreme cases seen here.

4.3. Run-up measurements

Fig. 11 shows the time series of different harmonic contributions to run-up in experiment #2, corresponding to the forces shown in Fig. 8. Fig. 11a, b, c, d plot run-up associated with the first-order generated wave field. The run-up as a result of the sub-harmonic error wave, can clearly be seen in Fig. 11d between $t = -4$ and -2 s. Fig. 11e, f, g, h plot the run-up time series associated with the second-order generated wave field. Similar to what has previously been seen in Fig. 8 for force measurements, the comparison of the harmonic contributions to run-up of both generation types in Fig. 11 shows that the significant difference is due to the presence of the sub-harmonic error wave.

Fig. 12 plots non-dimensionalised measured run-up induced by first- (FOG) and second-order (SOG) generated wave groups as a function of relative depth $k_0 d$ for eleven of the sixteen experimental cases (cases

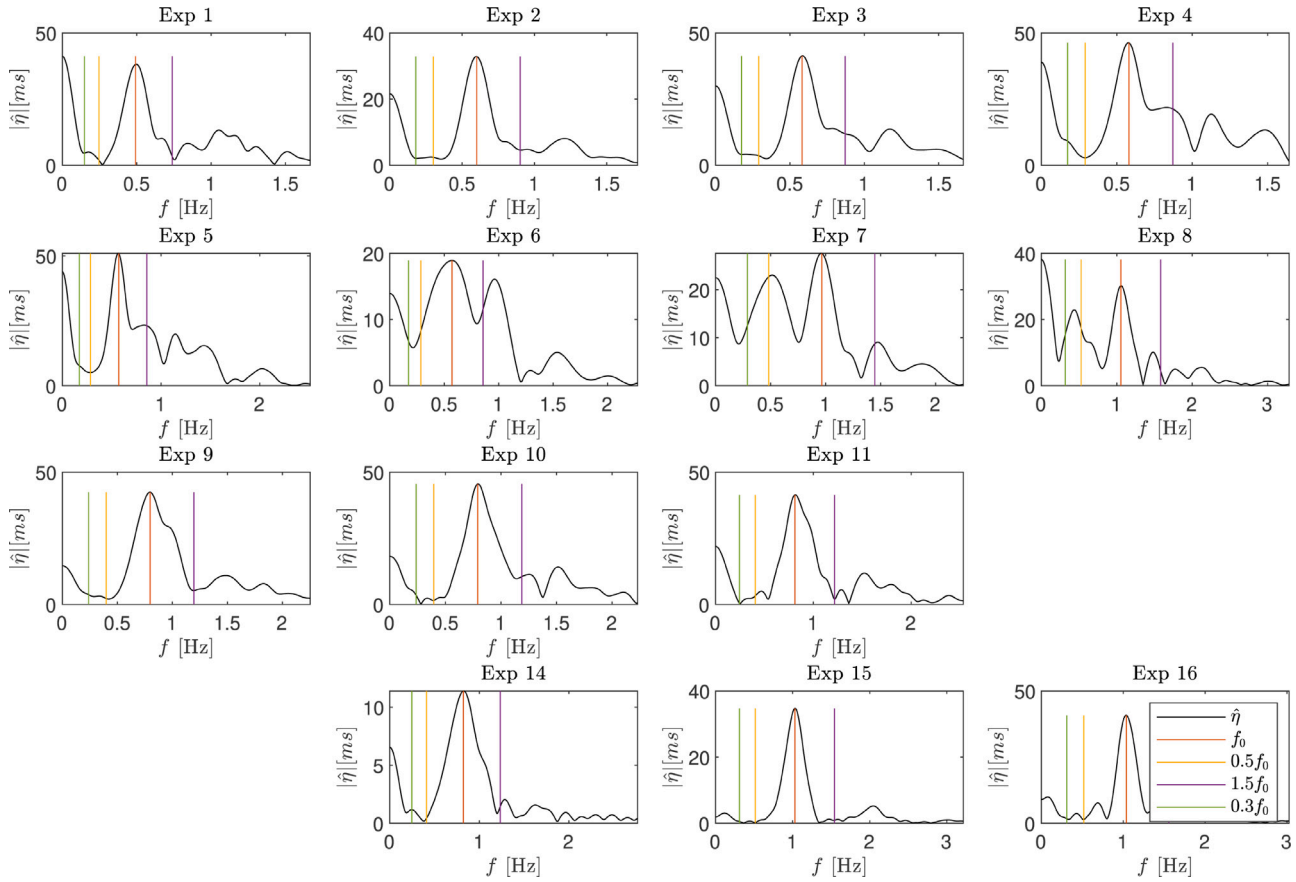

Fig. A.17. The magnitude of the Fourier transform of the padded time series of only the run-up at the wall, shown with the black line. The coloured lines show the harmonic separation windows. The red line denotes f_0, found using the maximum of the spectrum, yellow to purple lines are the linear part and the green line is the sub-harmonic cut-off frequency.

#6, 7, 8, 12 and 14 were omitted due to technical problems in the data acquisition). The mean of six phase repeats is plotted with the error bars indicating two standard deviations around the mean for each case. Each panel plots run-up associated with different group harmonics, with the theoretically predicted run-up indicated with a dashed black line. As seen previously with the similar plot for dynamic force, Fig. 12a presents the run-up for the first-order (linear) wave group of FOG and SOG cases. Here the run-up is the product of the amplitude of the incident and reflected group envelope, which when non-dimensionalised by wave steepness should be 2, indicated by the prediction line. The run-up for both FOG and SOG show reasonable agreement with the predictions at all water depths. Fig. 12b presents the sub-harmonic run-up. As expected, when water depth becomes shallower, the predicted run-up reduces due to the sub-harmonic set-down. Here, the SOG cases show good agreement with the predictions where as the FOG cases show poor agreement, particularly at shallow water depths due to the sub-harmonic error wave. Fig. 12c presents the super-harmonic run-up where SOG shows good agreement with the predictions at all water depths.

Fig. 13 plots the run-up induced at the centre of the wave group against the theoretical run-up. In panels a and b, the mean of all six phase repeats of each experimental case are plotted with two standard deviations indicated with error bars, where the mean is of the first-order group envelope which is then combined with the second-order free-surface elevation. In doing so, removing the phase dependence of each case. Fig. 13a plots the measured run-up for both FOG groups, in red, and SOG groups, in blue, against the theoretical second-order run-up according to our prediction. The black dashed line indicates one to one agreement between measured data and predictions. The plot shows that the second-order generated SOG cases have close agreement with the theory with the error bars of all but two cases overlapping the black dashed line. The measured first-order generated FOG cases are all greater than the theory predicts. This is important as the predicted run-up for a second-order generated case does not include contribution from the sub and super-harmonic free error waves. On average across all cases there is a 25% increase in run-up when using first-order generation; up to 67% increase for the shallowest cases. Fig. 13b plots the measured first-order generated run-up against the predictions of first-order generated run-up, where the predictions now include second-order sub- and super harmonic free error wave contributions. Here, we see that the first-order generated cases all overlap the black dashed line which indicates perfect agreement. Fig. 13c plots the predictions of run-up according to Goda's (1975) formula for run-up, where first-order generated and second-order generated offshore wave heights are used as the input for the formula. The values of both predictions are then plotted against the second-order corrected run-up predictions. Here, we see that using a measured first-order input, which has the free error waves within it, gives a significantly greater run-up prediction than if a second-order generated input is used, which does not include free error waves. Across all predictions given by Goda's formula, there is an average increase of 31% when using a first-order input; up to 64% for the shallowest cases.

5. Conclusions

In the present work we have experimentally investigated the implications of using second-order wave generation for wave structure interactions. In addition, we have derived narrow-banded theoretical solutions, which predict measurements well. We have examined the

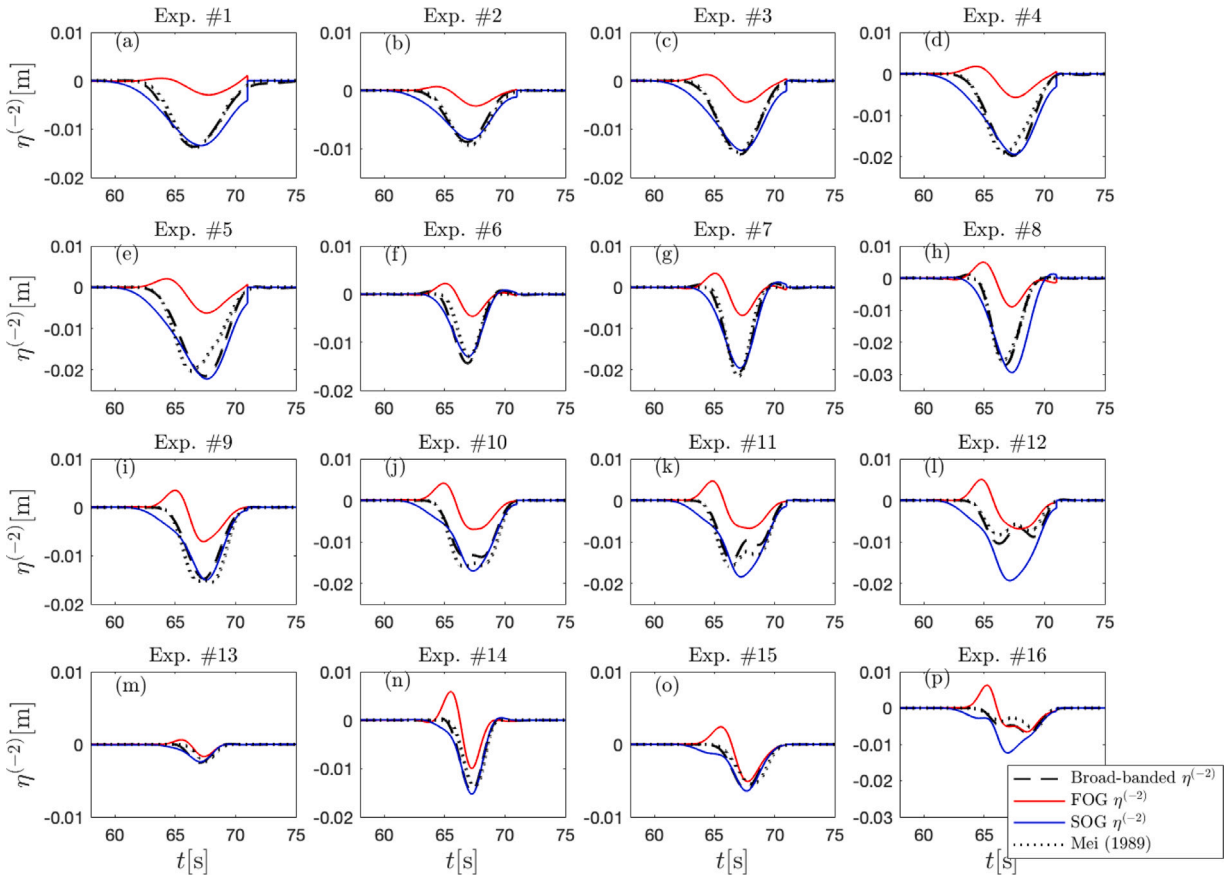

Fig. C.18. The measured sub-harmonic free-surface of all first-order generated (FOG) and second-order generated (SOG) experiments with a theoretical broad-banded subharmonic and the narrow-banded subharmonic given by Mei (1989). Results are measured at the location of WG 1.

difference in run-up and dynamic wave force on a vertical wall when using first- and second-order wave generation theory to create focused wave groups. Focused wave groups were selected as they offer a multi-frequency wave field in a short-duration, minimising the influence of wave reflections in the experimental setup.

Building on the numerical findings of Orszaghova et al. (2014), we have found that without correct application of second-order wave generation for wave-structure interaction experiments, the measured wave run-up and forces are significantly higher than they should be due to the preceding sub-harmonic error wave. Moreover, we show that using the measured offshore free-surface elevation, and propagating each harmonic contribution at its respective phase speed to the location of the vertical wall (where we assume full reflection and include interactions between incident and reflected wave groups), we are able to predict the dynamic wave force and run-up with a high degree of accuracy.

The assumption in our theoretical solutions of complete wave reflection at the vertical wall is shown to be valid, as we are able to recreate the measured incident and reflected wave fields, as well as predict run-up and force with good agreement. The interactions between incoming and reflected wave groups are important, as they result in an increase in the run-up.

The findings of the present work are important to consider before experimental results, generated according to first-order wave generation theory, are used to inform structure designs. Not accounting for second-order error waves in such scenario could lead to greater expected wave-induced run-up and force and subsequently, overly conservative design parameters. In the context of expected increasing hostility of conditions due to climate change, a level of conservatism regarding designs may be beneficial. Yet, the increase in run-up and force measurements given by the sub-harmonic error wave is erroneous and should therefore be compensated for in all wave-structure interaction experiments, particularly in shallow water depths.

CRediT authorship contribution statement

William Mortimer: Conceptualisation, Data Collection, Curation, and Analysis, Writing – original draft and editing. **Ross Calvert:** Investigation, Writing – reviewing and editing. **Alessandro Antonini:** Supervision, Reviewing. **Deborah Greaves:** Supervision. **Alison Raby:** Conceptualization, Methodology, Writing – reviewing and editing. **Ton S. van den Bremer:** Conceptualization, Visualization, Methodology, Writing – reviewing and editing.

Declaration of competing interest

The authors declare that they have no known competing financial interests or personal relationships that could have appeared to influence the work reported in this paper.

Data availability

Data will be made available on request.

Acknowledgements

The authors acknowledge support from Edinburgh Designs Ltd, who have donated their prototype wavemaker as part of ongoing collaborative developments. We would like to thank A. Oxenham, K. Monk and A. Reynolds at the COAST laboratory for help setting up the experiment. W.M Ph.D. studentship was funded by the COAST

Laboratory, T.S.vdB was supported by a Royal Academy of Engineering, UK, Research Fellowship.

Appendix A. Raw time series, processing, and quality control

A.1. Free-surface elevation

The free-surface elevation at WG 1 of all 16 experiments are shown in Fig. A.14 for the zero phase shift ($\varphi = 0°$). The time series at WG 1 are truncated to only include the incoming wave group. However, the signal does not go to zero after the incoming group due to reflections. This affects the spectrum seen in Fig. A.15, which have significant sub-harmonic energy corresponding to a mean in the time series. The correct carrier frequency f_0 is always the largest peak in spectra, but there are often significant peaks at other frequencies. The linear and sub-harmonic filters between the coloured bands in Fig. A.15 correspond to the time series in Fig. A.14.

A.2. Run-up on vertical wall

The video camera recorded the run-up against the wall for only 10 s before and during the peak run-up due to memory restrictions when using the high-speed camera. However, the window did not always capture the tail end of the group, as can be seen in Fig. A.16. In order to separate orders in steepness, the time series was padded out with zeros, and frequency-filtering of the spectrum is illustrated in Fig. A.17, which resulted in the linear and sub-harmonic run-up in Fig. A.16. The separation of the linear group is successful. However, the sometimes asymmetric and short time series resulted in difficulty when examining the sub-harmonic component. The short time series affects the lowest frequencies, and the asymmetry results in spurious negative signals, which are shifted towards the front of the group. Note that there is no run-up data for experiments 12 or 13.

To compare the sub-harmonic part to theoretical predictions, visual quality control of all experiments and phases was carried out. Experiments 6, 7, and 8 were eliminated because the high bandwidth combined with the short time series length for run-up (10 s) did not allow for successful processing. The values of the sub-harmonic run-up at the centre of the group, defined by the maximum of the linear envelope, were compared to theory to avoid any errors from the asymmetry.

Appendix B. Predicted run-up and force on a vertical wall by Goda (1975)

A widely used method to calculate wave force on a vertical wall is given by Goda (1975), originally developed for caisson breakwaters in Japan. The calculation integrates three predicted pressures, p_1, p_2 and p_3 over a trapezoidal distribution, with the maximum pressure p_1 at the still water level, p_2 at the extent of the maximum run-up and p_3 at the base of the vertical wall. The maximum predicted run-up is given by Goda (1975) as,

$$\eta_{\mathrm{w,Goda}} = 0.75(1+\cos\beta)H, \tag{B.1}$$

where β is the angle of incidence, equal to zero in our case, and H is the maximum offshore wave height. Due to the perpendicular angle of incidence in the present experiments, this simplifies to $\eta_{\mathrm{w,Goda}} = 1.5H$. Herein, H is measured at WG 1, and given as a summation of the first-order group envelope and second-order super-harmonic envelope and sub-harmonic set-down contributions. This is done to remove the phase dependence of the wave group. The component pressures given by Goda (1975) are,

$$\begin{aligned} p_1 &= \frac{1}{2}(1+\cos\beta)(\alpha_1+\alpha_2\cos^2\beta)\rho g H, \\ p_2 &= \frac{p_1}{\cosh(2\pi d/\lambda_0)}, \\ p_3 &= \alpha_3 p_1, \end{aligned} \tag{B.2}$$

where $\lambda_0 = 2\pi/k_0$ is the wave length associated with the carrier wave frequency. The coefficients α_1, α_2 and α_3 are given by Goda (2010) as,

$$\begin{aligned} \alpha_1 &= 0.6 + \frac{1}{2}\left[\frac{4\pi d/\lambda_0}{\sinh(4\pi d/\lambda_0)}\right]^2, \\ \alpha_2 &= \min\left(\frac{d_b-d}{3d_b}\left(\frac{H}{d}\right)^2\frac{2d}{H}\right), \\ \alpha_3 &= 1-\frac{d'}{d}\left[1-\frac{1}{\cosh(2\pi d/\lambda)}\right], \end{aligned} \tag{B.3}$$

where d_b is the water depth at the base of the wall and d' is the offshore water depth, here both equal to d.

The maximum force on the wall predicted by Goda's formula F_{Goda} is obtained by integrating p_1, p_2 and p_3 over a trapezoidal distribution, providing the wall height exceeds $\eta_{\mathrm{w,Goda}}$, as,

$$F_{\mathrm{Goda}}/b = \frac{1}{2}(p_2)\eta_{\mathrm{w,Goda}} + \frac{1}{2}(p_1+p_3)d. \tag{B.4}$$

Appendix C. Narrow and broad-banded subharmonic comparison

Fig. C.18 compares the measured FOG and SOG result of all sixteen experimental cases with the narrow-banded theoretical second-order sub-harmonic free surface given by Mei (1989) and the corresponding broad-banded free surface, which is given as the wave-averaged free-surface of a broad banded group in Longuet-Higgins and Stewart (1964), we use the implementation in Dalzell (1999) as also used in McAllister et al. (2018). Fig. C.18, demonstrates a good agreement between the broad-banded theoretical subharmonic and the majority of the sixteen second-order generated (SOG) experimental cases.

References

Allsop, N.W.H., Vicinanza, D., McKenna, J.E., 1996. Wave Forces on Vertical and Composite Breakwaters. HR Wallingford Wallingford, UK.

Antonini, A., Archetti, R., Lamberti, A., 2017. Wave simulation for the design of an innovative quay wall: The case of Vlorë Harbour. Nat. Hazards Earth Syst. Sci. 127–142.

Antonini, A., Brownjohn, J.M.W., Dassanayake, D., Raby, A., Bassit, J., Pappas, A., D'Ayala, D., 2021. A Bayesian inverse dynamic approach for impulsive wave loading reconstruction: Theory, laboratory and field application. Coast. Eng. 103920.

Baldock, T.E., Huntley, D.A., Bird, P.A.D., O'hare, T., Bullock, G.N., 2000. Breakpoint generated surf beat induced by bichromatic wave groups. Coast. Eng. 39 (2–4), 213–242.

Baldock, T.E., Swan, C., Taylor, P.H., 1996. A laboratory study of nonlinear surface waves on water. Phil. Trans. R. Soc. A 354 (1707), 649–676.

Barthel, V., Mansard, E.P.D., Sand, S.E., Vis, F.C., 1983. Group bounded long waves in physical models. Ocean Eng. 10 (4), 261–294.

Battjes, J.A., Bakkenes, H.J., Janssen, T.T., van Dongeren, A.R., 2004. Shoaling of subharmonic gravity waves. J. Geophys. Res.: Oceans 109 (C2).

Boccotti, P., 1983. Some new results on statistical properties of wind waves. Appl. Ocean Res. 5 (3), 134–140.

Borthwick, A.G.L., Hunt, A.C., Feng, T., Taylor, P.H., Stansby, P.K., 2006. Flow kinematics of focused wave groups on a plane beach in the UK coastal research facility. Coast. Eng. 53 (12), 1033–1044. http://dx.doi.org/10.1016/j.coastaleng.2006.06.007.

Calvert, R., Whittaker, C., Raby, A., Taylor, P.H., Borthwick, A.G.L., van den Bremer, T.S., 2019. Laboratory study of the wave-induced mean flow and set-down in unidirectional surface gravity wave packets on finite water depth. Phys. Rev. Fluids 4 (11), 114801.

Cuomo, G., 2005. Dynamics of wave-induced loads and their effects on coastal structures. Final Dissertation PhD in Science of Civil Engineering, University of Roma TRE, Italy.

Cuomo, G., Allsop, W., Bruce, T., Pearson, J., 2010. Breaking wave loads at vertical seawalls and breakwaters. Coast. Eng. 57 (4), 424–439.

Dalzell, J.F., 1999. A note on finite depth second-order wave–wave interactions. Appl. Ocean Res. 21 (3), 105–111.

Dassanayake, D., Raby, A., Antonini, A., 2019. Physical modelling of the effect of shoal geometry on wave loading and runup on a cylinder. In: Coastal Structures 2019. pp. 211–220.
Dawson, D., Shaw, J., Gehrels, W.R., 2016. Sea-level rise impacts on transport infrastructure: The notorious case of the coastal railway line at Dawlish, England. J. Transp. Geogr. 51, 97–109.
Eldrup, M.R., Andersen, T.L., 2019. Estimation of incident and reflected wave trains in highly nonlinear two-dimensional irregular waves. J. Waterw. Port Coast. Ocean Eng. 145 (1), 04018038.
Fang, Q., Liu, J., Guo, A., Li, H., 2020. Methodology and experimental validation for generating periodic focused waves in a wave flume. Ocean Eng. 210, 107394.
Fenton, J.D., 1985. Wave forces on vertical walls. J. Waterw. Port Coast. Ocean Eng. 111 (4), 693–718.
Goda, Y., 1975. New wave pressure formulae for composite breakwaters. In: Coastal Engineering 1974. pp. 1702–1720.
Goda, Y., 2010. Random Seas and Design of Maritime Structures, vol. 33. World Scientific Publishing Company.
Haigh, I.D., Nicholls, R.J., Penning-Roswell, E., Sayers, P., 2020. Impacts of climate change on coastal flooding, relevant to the coastal and marine environment around the UK. MCCIP Science Review 2020 546–565.
Hofland, B., Wenneker, I., Van Steeg, P., 2014. Short test durations for wave overtopping experiments. In: Proceedings of the 5th International Conference on the Application of Physical Modelling to Port and Coastal Protection. pp. 349–358.
Hunt, A., 2003. Extreme Waves, Overtopping and Flooding at Sea Defences (Ph.D. thesis). University of Oxford.
IPCC, 2019. Technical summary: IPCC special report on the ocean and cryosphere in a changing climate.
Janssen, T.T., Battjes, J.A., Van Dongeren, A.R., 2003. Long waves induced by short-wave groups over a sloping bottom. J. Geophys. Res.: Oceans 108 (C8).
Karmpadakis, I., Swan, C., 2020. On the average shape of the largest waves in finite water depths. J. Phys. Oceanogr. 50 (4), 1023–1043.
Klopman, G., Van Leeuwen, P.J., 1990. An efficient method for the reproduction of non-linear random waves. In: Proceedings of the 22nd Coastal Engineering, Delft 1990. pp. 478–488.
Laface, V., Malara, G., Kougioumtzoglou, I.A., Romolo, A., Arena, F., 2018. Nonlinear wave crest distribution on a vertical breakwater. Coast. Eng. 138, 227–234. http://dx.doi.org/10.1016/j.coastaleng.2018.04.018.
Longuet-Higgins, M.S., Stewart, R.W., 1962. Radiation stress and mass transport in gravity waves, with application to 'surf beats'. J. Fluid Mech. 13 (4), 481–504.
Longuet-Higgins, M.S., Stewart, R.W., 1964. Radiation stresses in water waves; a physical discussion, with applications. In: Deep Sea Research and Oceanographic Abstracts, vol. 11. (4), Elsevier, pp. 529–562.
Martins, K., Bonneton, P., Michallet, H., 2021. Dispersive characteristics of non-linear waves propagating and breaking over a mildly sloping laboratory beach. Coast. Eng. 167, 103917.
McAllister, M.L., Adcock, T.A.A., Taylor, P.H., Van Den Bremer, T.S., 2018. The set-down and set-up of directionally spread and crossing surface gravity wave groups. J. Fluid Mech. 835, 131–169.
McAllister, M.L., van den Bremer, T.S., 2019. Lagrangian measurement of steep directionally spread ocean waves: Second-order motion of a wave-following measurement buoy. J. Phys. Oceanogr. 49 (12), 3087–3108. http://dx.doi.org/10.1175/JPO-D-19-0170.1.
Van der Meer, J.W., Allsop, N.W.H., Bruce, T., De Rouck, J., Kortenhaus, A., Pullen, T., Schüttrumpf, H., Troch, P., Zanuttigh, B., 2018. EurOtop: Manual on wave overtopping of sea defences and related structures: An overtopping manual largely based on European research, but for worldwide application.
Mei, C.C., 1989. The Applied Dynamics of Ocean Surface Waves, vol. 1. World scientific.
Mortimer, W., Raby, A., Antonini, A., Greaves, D., van den Bremer, T.S., 2022. Correct generation of the bound set-down for surface gravity wave groups in laboratory experiments of intermediate to shallow depth. Coast. Eng. 174, 104121.
Moura, T., Baldock, T.E., 2019. The influence of free long wave generation on the shoaling of forced infragravity waves. J. Mar. Sci. Eng. 7 (9), 305.
Orszaghova, J., Taylor, P.H., Borthwick, A.G.L., Raby, A.C., 2014. Importance of second-order wave generation for focused wave group run-up and overtopping. Coast. Eng. 94, 63–79.
Oumeraci, H., Kortenhaus, A., Allsop, W., de Groot, M., Crouch, R., Vrijling, H., Voortman, H., 2001. Probabilistic Design Tools for Vertical Breakwaters. CRC Press.
Pullen, T., Allsop, N.W.H., Bruce, T., Kortenhaus, A., Schüttrumpf, H., Van der Meer, J.W., 2007. EurOtop Wave Overtopping of Sea Defences and Related Structures: Assessment Manual.
Romolo, A., Arena, F., 2008. Mechanics of nonlinear random wave groups interacting with a vertical wall. Phys. Fluids 20 (3), 036604.
Romolo, A., Arena, F., 2013. Three-dimensional non-linear standing wave groups: Formal derivation and experimental verification. Int. J. Non-Linear Mech. 57, 220–239.
Schäffer, H.A., 1996. Second-order wavemaker theory for irregular waves. Ocean Eng. 23 (1), 47–88.
Sorensen, R.M., 2005. Basic Coastal Engineering, vol. 10. Springer Science & Business Media.
Sriram, V., Schlurmann, T., Schimmels, S., 2015. Focused wave evolution using linear and second-order wavemaker theory. Appl. Ocean Res. 53, 279–296.
Sun, Y., Zhang, X., 2017. A second order analytical solution of focused wave group interacting with a vertical wall. Int. J. Nav. Archit. Ocean Eng. 9 (2), 160–176. http://dx.doi.org/10.1016/j.ijnaoe.2016.09.002.
Taherkhani, M., Vitousek, S., Barnard, P.L., Frazer, N., Anderson, T.R., Fletcher, C.H., 2020. Sea-level rise exponentially increases coastal flood frequency. Sci. Rep. 10 (1), 1–17.
Takahashi, S., 2002. Design of Vertical Breakwaters. Reference Document No. 34, Port and Harbour Research Institute, Japan.
Taylor, P.H., Williams, B.A., 2004. Wave statistics for intermediate depth water - NewWaves and symmetry. J. Offshore Mech. Arct. Eng. 126 (1), 54–59.
Tromans, P.S., Anaturk, A.R., Hagemeijer, P., 1991. A new model for the kinematics of large ocean waves-application as a design wave. In: Proceedings of the First International Offshore and Polar Engineering Conference, vol. 3. International Society of Offshore and Polar Engineers, pp. 64–71.
van den Bremer, T.S., Whittaker, C., Calvert, R., Raby, A., Taylor, P.H., 2019. Experimental study of particle trajectories below deep-water surface gravity wave groups. J. Fluid Mech. 879, 168–186.
Van Dongeren, A., Reniers, A., Battjes, J., Svendsen, I., 2003. Numerical modeling of infragravity wave response during DELILAH. J. Geophys. Res.: Oceans 108 (C9).
Van Leeuwen, P.J., Klopman, G., 1996. A new method for the generation of second-order random waves. Ocean Eng. 23 (2), 167–192.
Vousdoukas, M.I., Mentaschi, L., Hinkel, J., Ward, P.J., Mongelli, I., Ciscar, J.-C., Feyen, L., 2020. Economic motivation for raising coastal flood defenses in Europe. Nature Commun. 11 (1), 1–11.
Whittaker, C.N., Fitzgerald, C.J., Raby, A.C., Taylor, P.H., Borthwick, A.G.L., 2018. Extreme coastal responses using focused wave groups: Overtopping and horizontal forces exerted on an inclined seawall. Coast. Eng. 140, 292–305.
Whittaker, C.N., Fitzgerald, C.J., Raby, A.C., Taylor, P.H., Orszaghova, J., Borthwick, A.G.L., 2017. Optimisation of focused wave group runup on a plane beach. Coast. Eng. 121 (November 2016), 44–55.
Whittaker, C.N., Raby, A.C., Fitzgerald, C.J., Taylor, P.H., 2016. The average shape of large waves in the coastal zone. Coast. Eng. 114, 253–264.
Young, I.R., Ribal, A., 2019. Multiplatform evaluation of global trends in wind speed and wave height. Science 364 (6440), 548–552.